

Cite this: *Chem. Sci.*, 2025, 16, 7695

All publication charges for this article have been paid for by the Royal Society of Chemistry

# Insight into the atomic-level structure of $\gamma$ -alumina using a multinuclear NMR crystallographic approach†

M. Bonifac Legrady,<sup>‡</sup> Daniel M. Dawson,<sup>Ⓜ</sup> Paul B. Webb<sup>Ⓜ</sup> and Sharon E. Ashbrook<sup>Ⓜ</sup>\*

The combination of multinuclear NMR spectroscopy with  $^{17}\text{O}$  isotopic enrichment and DFT calculations provided detailed insight into both the bulk and surface structure of  $\gamma\text{-Al}_2\text{O}_3$ . Comparison of experimental  $^{17}\text{O}$  NMR spectra to computational predictions confirmed that bulk  $\gamma\text{-Al}_2\text{O}_3$  contains Al cations primarily in “spinel-like” sites, with roughly equal numbers of alternating  $\text{Al}^{\text{VI}}$  and  $\text{Al}^{\text{IV}}$  vacancies in disordered “chains”. The work showed that overlap of signals from  $\text{O}^{\text{IV}}$  and  $\text{O}^{\text{III}}$  species complicates detailed spectral analysis and highlighted potential problems with previous work where structural conclusions are based on an unambiguous assignment (and quantification) of these signals. There was no evidence for the presence of H, or for any significant levels of O vacancies, in the bulk structure of  $\gamma\text{-Al}_2\text{O}_3$ . Computational predictions from structural models for different surfaces showed a wide variety of protonated and non-protonated O species occur. Assignment of signals for two types of protonated O species was achieved using variable temperature CP and TRAPDOR experiments, with the sharper and broader resonances attributed to more accessible surface sites that interact more strongly with water and less accessible aluminols, respectively. DFT-predicted  $^1\text{H}$  NMR parameters confirmed the  $^1\text{H}$  shift increases with denticity but is also dependent on the coordination number of the next nearest neighbour Al species. Spectral assignments were also supported by  $^1\text{H}\text{-}^{27}\text{Al}$  RESPDOR experiments, which identified spectral components resulting from  $\mu_1$ ,  $\mu_2$  and  $\mu_3$  aluminols. Combining these with  $^1\text{H}\text{-}^{27}\text{Al}$  D-HMQC experiments showed that (i)  $\mu_1$  aluminols are more likely to be bound to  $\text{Al}^{\text{IV}}$ , (ii)  $\mu_2$  aluminols are coordinated to all three types of Al, but with a higher proportion bound to similar types of Al and (iii)  $\mu_3$  aluminols are most likely bound to higher coordinated Al species.  $^1\text{H}$  DQ MAS spectroscopy confirmed no aluminols exist exclusively in isolation but showed that the closest proximities are between bridging aluminols coordinated to  $\text{Al}^{\text{IV}}$  and/or  $\text{Al}^{\text{V}}$  species.

Received 15th February 2025  
Accepted 10th March 2025

DOI: 10.1039/d5sc01198a

rsc.li/chemical-science

## Introduction

Transition aluminas ( $\text{Al}_2\text{O}_3$ ) are among the most widely used oxides in heterogeneous catalysis.<sup>1</sup> Alumina is employed as a support material for processes including methanol production and Fischer–Tropsch synthesis, and can be used to catalyse transformations such as alcohol dehydration, skeletal isomerisation or the removal of sulfur from gases in the Claus process.<sup>2–6</sup> The versatility of aluminas can be attributed primarily to a high mechanical and chemical stability, high surface area and porosity, and the Lewis-acidity of coordinatively unsaturated surface Al sites. Yet despite their

industrial importance, the atomic-scale surface, sub surface and bulk structure of these materials is not well understood.

There are many alumina polymorphs or “forms”,<sup>7</sup> typically denoted by Greek letters, with the most thermodynamically stable being  $\alpha\text{-Al}_2\text{O}_3$ . Aluminas can be categorised into two types based on the arrangement of oxygens in the structure, with a hexagonal close packed (hcp) array for the  $\alpha$ ,  $\kappa$  and  $\chi$  forms and a face centred cubic close packed (fcc) array for the  $\eta$ ,  $\gamma$ ,  $\delta$  and  $\theta$  forms.<sup>4,7–11</sup> The distinct forms are then further distinguished by different arrangements of the Al cations.  $\gamma\text{-Al}_2\text{O}_3$  is one of the most studied transition aluminas, yet its precise structure is still the subject of considerable and ongoing debate, with several different models proposed in the literature.

$\gamma\text{-Al}_2\text{O}_3$  is often described as a non-stoichiometric or defect spinel,<sup>12,13</sup> with a cubic unit cell that contains cation vacancies to maintain charge neutrality, although consensus on the preferential location of the vacancies (*i.e.*, on tetrahedral or octahedral sites) and on any clustering or ordering has yet to be reached. A number of computational studies determined it was

School of Chemistry, EaStCHEM and Centre of Magnetic Resonance, University of St Andrews, North Haugh, St Andrews KY16 9ST, UK. E-mail: sema@st-andrews.ac.uk

† Electronic supplementary information (ESI) available. See DOI: <https://doi.org/10.1039/d5sc01198a>

‡ Currently at: School of Chemistry, University of Southampton, University Road, Southampton, SO17 1BJ, UK.



energetically most favourable to locate vacancies on the octahedral ( $\text{Al}^{\text{VI}}$ ) sites with maximum separation between them.<sup>11,14–20</sup> However, other authors concluded from molecular dynamics (MD) simulations that cation vacancies are located at tetrahedral ( $\text{Al}^{\text{IV}}$ ) sites,<sup>21</sup> while Lee *et al.* suggested vacancies were present on both types of sites ( $\sim 63\%$   $\text{Al}^{\text{IV}}$  and  $\sim 37\%$   $\text{Al}^{\text{VI}}$ ).<sup>22</sup> Many experimental studies have also tried to resolve this controversy, with results from X-ray diffraction (XRD), electron microscopy and  $^{27}\text{Al}$  NMR spectroscopy suggesting vacancies were located exclusively on  $\text{Al}^{\text{VI}}$  sites,<sup>23–28</sup> while other electron diffraction and NMR studies have been interpreted as evidence for vacancies occurring at  $\text{Al}^{\text{IV}}$  sites.<sup>29–33</sup> Some diffraction-based studies have also reported tetragonal distortions of the cubic unit cell.<sup>13,29,34,35</sup> It has also been suggested from diffraction data that  $\text{Al}^{3+}$  cations could occupy non-spinel interstitial positions (although there is also some debate over whether these are  $\text{Al}^{\text{IV}}$  or  $\text{Al}^{\text{VI}}$  sites),<sup>36,37</sup> while work from Paglia *et al.* (using primarily diffraction, microscopy and computation) proposed a tetragonal model for bulk  $\gamma\text{-Al}_2\text{O}_3$ , with over 40% of the  $\text{Al}^{3+}$  cations occupying  $\text{Al}^{\text{VI}}/\text{Al}^{\text{IV}}$  non-spinel sites.<sup>35</sup> A different non-spinel model, derived from MD simulations and exhibiting a monoclinic unit cell was described by Krokidis.<sup>38</sup>

Surprisingly few detailed NMR studies have been carried out on  $\gamma\text{-Al}_2\text{O}_3$ , likely reflecting the challenges associated with highly disordered materials.<sup>39</sup> The majority that have been performed have largely focussed on  $^{27}\text{Al}$  NMR, drawing conclusions from the relative intensities of the  $\text{Al}^{\text{IV}}$  and  $\text{Al}^{\text{VI}}$  signals in magic-angle spinning (MAS) NMR spectra.<sup>38,40</sup> Although the  $^{27}\text{Al}$  chemical shift depends strongly on coordination number, the broadening arising from the quadrupolar interaction, and as a result of disorder, often limits the extraction of precise parameters, particularly at the lower  $B_0$  field strengths used in earlier work.<sup>39</sup> It has also been shown that the  $^{27}\text{Al}$  MAS NMR spectrum can vary with the methods used for sample preparation, the particle size, surface area and hydration state.<sup>38,40</sup> However, the nature of the cation site (*i.e.*, spinel or non-spinel) is not easily determined from the  $^{27}\text{Al}$  NMR spectrum (as the immediate local environments in these two are very similar), with cation vacancies occurring only in the second coordination sphere, resulting in a more minor variation in the NMR parameters through small changes in the positions of the neighbouring  $\text{O}^{2-}$  anions. In contrast, the local geometry around the  $\text{O}^{2-}$  anions changes significantly with neighbouring cation vacancies, and the arrangement of the surrounding  $\text{Al}^{3+}$  cations depends crucially upon whether they occupy spinel or non-spinel positions in the structure. Given the low natural abundance of the NMR-active  $^{17}\text{O}$  isotope (0.037%), and the cost and practical challenges associated with isotopic enrichment,<sup>41</sup>  $^{17}\text{O}$  NMR spectroscopy of alumina has been much less common,<sup>42–47</sup> although early work was performed by Walter and Oldfield (as discussed later).<sup>42</sup> Perhaps of most note, is recent high-field NMR work using double-quantum NMR spectroscopy to identify different types of surface and sub surface species, which indicated a non-random distribution of O species, but used the earlier assignment of the signals proposed by Walter and Oldfield.<sup>43</sup>

In this work we combine multinuclear ( $^1\text{H}$ ,  $^{17}\text{O}$  and  $^{27}\text{Al}$ ) and multidimensional NMR spectroscopy of  $\gamma\text{-Al}_2\text{O}_3$  with periodic

planewave density functional theory (DFT) calculations of potential structural models of the bulk and surface structure to gain insight into the atomic-scale structure of this important, yet poorly understood, material. This NMR crystallographic approach is vital for interpreting the spectroscopic signals observed and showing that these can often result from an overlap of resonances from different crystallographic environments, which has hindered spectral assignment in previous work. We show that  $^{17}\text{O}$  NMR spectroscopy is a sensitive probe of the detailed local structure, and of the surface structure in particular, providing, when combined with computation, one of the most successful approaches to date for structural characterisation of this industrially important material.

## Methodology

### Synthesis and isotopic enrichment

Commercial boehmite-derived  $\gamma\text{-Al}_2\text{O}_3$  was obtained from Sasol UK Ltd (brand name Puralox) and used either as received, after dehydration or after  $^{17}\text{O}$  enrichment. Samples were dehydrated at 150–300 °C by heating 150 mg in a quartz vial in a sand bath on a hotplate. For dehydration at higher temperatures 100–200 mg of sample was transferred into a quartz vial and heated under vacuum at 500 or 700 °C for 12–24 h in a tube furnace. After dehydration, samples were packed into commercial  $\text{ZrO}_2$  rotors in a glovebox under an inert  $\text{N}_2$  atmosphere. Isotopic enrichment was carried using post-synthetic exchange with 70%  $^{17}\text{O}_2$  (g). Approximately 150 mg of sample was transferred into a quartz vial and immersed in liquid  $\text{N}_2$ , before exposure to  $^{17}\text{O}_2$  (g), which then condensed in the pores. The vial was then returned to room temperature, placed in a tube furnace and heated at a temperature between 500 and 950 °C for 12–72 h. Samples isotopically enriched at  $X$  °C will be referred to as  $\gamma\text{-Al}_2^{17}\text{O}_3(X^\circ\text{C})$  throughout. Although the absolute level of enrichment was not measured directly, this is estimated to be  $\sim 25\text{--}30\%$  by comparison to materials with known enrichment levels.

### NMR spectroscopy

Solid-state NMR spectra were acquired either in house using Bruker Avance III instruments equipped with 9.4 or 14.1 T wide-bore magnets, at the Scottish High-field NMR facility using a Bruker Avance NEO spectrometer equipped with a standard-bore 18.8 T magnet, or at the UK High-Field NMR facility using a Bruker Avance III spectrometer equipped with a 20.0 T wide-bore magnet. Powdered samples were packed into  $\text{ZrO}_2$  rotors and rotated at MAS rates of 5–40 kHz or using conventional double- or triple-resonance probes. NMR spectra are shown referenced relative to  $\text{H}_2\text{O}(\text{l})$  for  $^{17}\text{O}$ , 1 M  $\text{Al}(\text{NO}_3)_3$  (aq) for  $^{27}\text{Al}$  (determined using a secondary reference of aluminium acetylacetonate ( $\delta_{\text{iso}} = 0$  ppm)) and TMS for  $^1\text{H}$  (determined using a secondary reference of L-alanine ( $\delta(\text{NH}_3^+) = 8.5$  ppm)). Spectra were acquired at ambient temperature unless otherwise stated. High-resolution NMR spectra were acquired using MQMAS<sup>48</sup> ( $^{27}\text{Al}$ ) and DQF-STMAS<sup>49,50</sup> ( $^{17}\text{O}$ ) experiments. For more detailed experimental parameters see figure captions and Section S1 in the ESI.†



## Computation

Periodic planewave DFT calculations were carried out using the CASTEP code (version 16.12).<sup>51–53</sup> Calculations were performed using the PBE exchange correlation functional<sup>54</sup> and the semi-empirical dispersion correction scheme of Tkatchenko and Scheffler.<sup>55</sup> Core-valence interactions were described by ultrasoft pseudopotentials, accounting for scalar relativistic effects using ZORA.<sup>56</sup> Planewave energy cutoffs of 45 or 60 Ry were used for geometry optimisation, and 60 Ry for all NMR calculations, with the first Brillouin zone sampled using a Monkhorst-Pack grid<sup>57</sup> with a reciprocal space grid spacing of  $0.04 \times 2\pi \text{ \AA}^{-1}$  in all cases. Initial structural models were generated by introducing vacancies into an undistorted  $(\text{Al}_3\text{O}_4)$  spinel structure and modified as described below. In the geometry optimization all atomic coordinates and unit cell parameters were allowed to vary for bulk models, while unit cell parameters were constrained for the surface models. Further models of bulk and surface structures were generated as described in the text and Sections S3–S6 of the ESI.†

NMR parameters were calculated using the gauge-including projector augmented wave (GIPAW<sup>51</sup>) approach to reconstruct the all-electron wavefunction in the presence of a magnetic field. Calculations provide the absolute shielding tensor ( $\sigma$ ),  $J$  coupling tensor ( $J$ ) or electric field gradient tensor ( $V$ ). Diagonalization provides their respective principal components, where  $\sigma_{11} \leq \sigma_{22} \leq \sigma_{33}$ ,  $J_{11} \leq J_{22} \leq J_{33}$  and  $|V_{xx}| \leq |V_{yy}| \leq |V_{zz}|$ . The isotropic shielding is given by  $\sigma_{\text{iso}} = (1/3)\text{Tr}(\sigma)$  and the predicted isotropic chemical shift by  $\delta_{\text{iso}} = \sigma_{\text{ref}} - \sigma_{\text{iso}}$ . Reference shieldings ( $\sigma_{\text{ref}}$ ) were determined by comparing experimental shift and calculated shielding for  $\alpha\text{-Al}_2\text{O}_3$  ( $^{27}\text{Al}$  and  $^{17}\text{O}$ ) and TMS ( $^1\text{H}$ ).<sup>42,58</sup> The quadrupolar coupling constant,  $C_Q = eQV_{zz}/h$  was obtained using nuclear quadrupole moments of 146.6 and  $-25.58 \text{ mb}$ , for  $^{27}\text{Al}$  and  $^{17}\text{O}$ , respectively.<sup>59</sup> From the quadrupolar magnitude,  $C_Q$ , and asymmetry,  $\eta_Q = (V_{xx} - V_{yy})/V_{zz}$ , the quadrupolar product  $P_Q = C_Q(1 + \eta_Q^2/3)^{1/2}$  can be determined. The isotropic  $J$  coupling is given by  $(1/3)\text{Tr}(J)$ .

Density matrix simulations were performed using SIMPSON.<sup>60</sup> Details on the spin systems considered and the parameters used are provided in Section S10 of the ESI.†

## Results and discussion

### $^{17}\text{O}$ NMR spectroscopy: bulk structure of $\text{Al}_2\text{O}_3$

Fig. 1 shows structural models for  $\gamma\text{-Al}_2\text{O}_3$  based on a cubic  $Fd\bar{3}m$  unit cell containing an fcc arrangement of  $\text{O}^{2-}$  anions (on the 32e Wyckoff positions), indicating both the spinel (8a and 16d) and non-spinel (48f and 16c) cation positions.<sup>13</sup> In a spinel structure without cation vacancies, every  $\text{O}^{2-}$  anion is tetrahedrally coordinated and surrounded by one  $\text{Al}^{\text{IV}}$  and three  $\text{Al}^{\text{VI}}$  cations (as shown in Fig. 1c). To aid the interpretation of local structure in the following discussion, this O environment will be denoted as  $\text{O}^{\text{IV}}(6664)$ . To maintain charge balance in the spinel-based model of  $\text{Al}_2\text{O}_3$ ,  $8/3 \text{ Al}^{3+}$  vacancies are needed for every 32  $\text{O}^{2-}$  anions. Introducing an  $\text{Al}^{\text{VI}}$  vacancy generates six three-coordinate O species (denoted  $\text{O}^{\text{III}}(664)$ ), while an  $\text{Al}^{\text{IV}}$  vacancy generates four  $\text{O}^{\text{III}}(666)$  sites. For non-spinel structures,

there are 11 48f and 16c cations around each  $\text{O}^{2-}$  potentially giving rise to many different O local environments, as seen in Fig. 1c.

Fig. 2a shows  $^{17}\text{O}$  MAS NMR spectra of  $\gamma\text{-Al}_2^{17}\text{O}_3$  (500 °C), enriched for 48 h and then left open to the atmosphere, at three different  $B_0$  field strengths. The increase in field strength (and the consequent reduction in the second-order quadrupolar broadening) increases the spectral resolution and enables approximately four oxygen signals to be distinguished. The two sharper resonances at higher shift have been suggested to correspond to non-protonated oxygen species, while the two broader signals at lower shift have been previously assigned to protonated oxygens (*i.e.*, adsorbed water and hydroxyl groups).<sup>42–45</sup> The signals from the non-protonated oxygens do not become significantly sharper at higher field, suggesting that the major contribution to the line broadening is a distribution of chemical shifts as a result of small variations in the local environments, rather than from a significant second-order quadrupolar interaction. Early  $^{17}\text{O}$  NMR of  $\gamma\text{-Al}_2\text{O}_3$  by Walter and Oldfield<sup>42</sup> assigned the non-protonated  $^{17}\text{O}$  signal at higher shift ( $\sim 70 \text{ ppm}$  at 20.0 T) to  $\text{O}^{\text{IV}}$  and that at  $\sim 55 \text{ ppm}$  (at 20.0 T) to  $\text{O}^{\text{III}}$ . Although this assignment is generally accepted in the literature,<sup>43–46</sup> it will be shown later that this is likely to be an oversimplification. However, the “ $\text{O}^{\text{IV}}$ ”: “ $\text{O}^{\text{III}}$ ” ratio (1 : 1) obtained from  $^{17}\text{O}$  spectra in early work was later used<sup>46</sup> to conclude that the cation vacancies in a spinel structure must be located exclusively at the octahedral positions (if they were at the tetrahedral sites, a 2 : 1 ratio would be obtained). This ratio

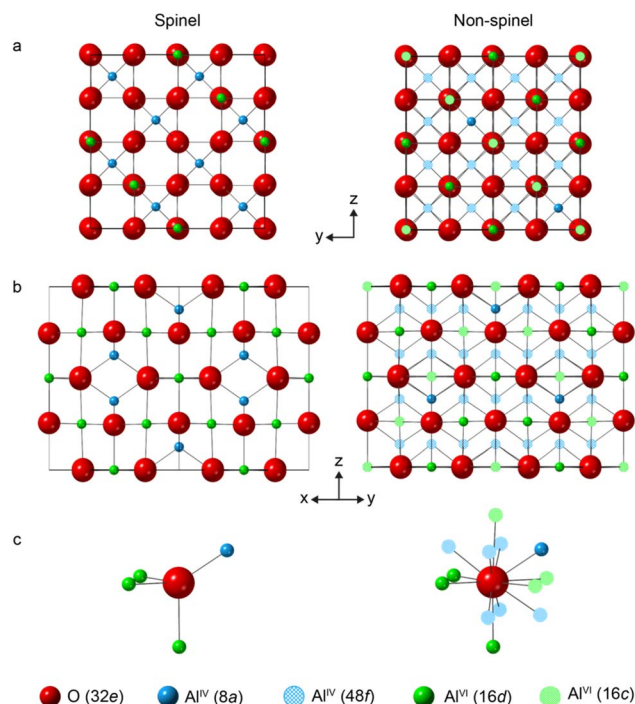


Fig. 1 Schematic models for the structure of  $\gamma\text{-Al}_2\text{O}_3$  based on a fcc arrangement of  $\text{O}^{2-}$  anions, and denoting the spinel and non-spinel cation positions, viewed (a) down the  $x$  axis and (b) down the  $(111)$  axis. (c) Local arrangement of the  $\text{Al}^{3+}$  cations around O in each of the models.



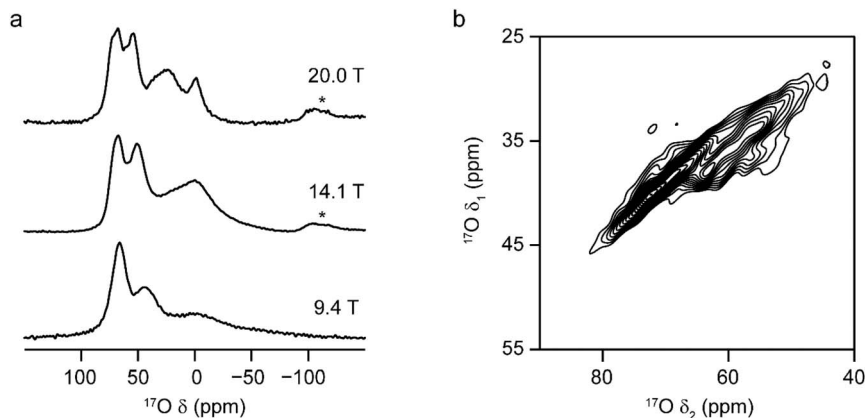


Fig. 2  $^{17}\text{O}$  NMR of  $\gamma\text{-Al}_2\text{O}_3$  enriched by post-synthetic exchange with  $^{17}\text{O}_2$  (g). (a) MAS NMR spectra of  $\gamma\text{-Al}_2^{17}\text{O}_3$  (500  $^\circ\text{C}$ ), acquired at the magnetic fields shown. (b)  $^{17}\text{O}$  (20.0 T, 30 kHz) DQF-STMAS<sup>49</sup> NMR spectrum of  $\gamma\text{-Al}_2^{17}\text{O}_3$  (950  $^\circ\text{C}$ ). For detailed experimental parameters see Section S1 of the ESI†

was obtained by fitting the spectrum using Gaussian line-shapes, *i.e.*, without considering the characteristic “tails” to low shift usually seen for quadrupolar nuclei in disordered environments,<sup>39</sup> and neglecting any effects of differential relaxation rates or differing nutation rates (*i.e.*, spectra were not acquired using a short flip angle pulse). Although the spectra in Fig. 2a in this work were acquired using sufficiently long recycle intervals

(see Section S1 of the ESI†), it should be noted that the material was isotopically enriched by post-synthetic exchange with  $^{17}\text{O}_2$  (g), leading to possible non-quantitative incorporation of  $^{17}\text{O}$ . Although we would expect any differences to be insignificant, particularly when higher temperatures are used, any detailed structural conclusions in this work should not be based on spectral signal intensities alone but from the range and

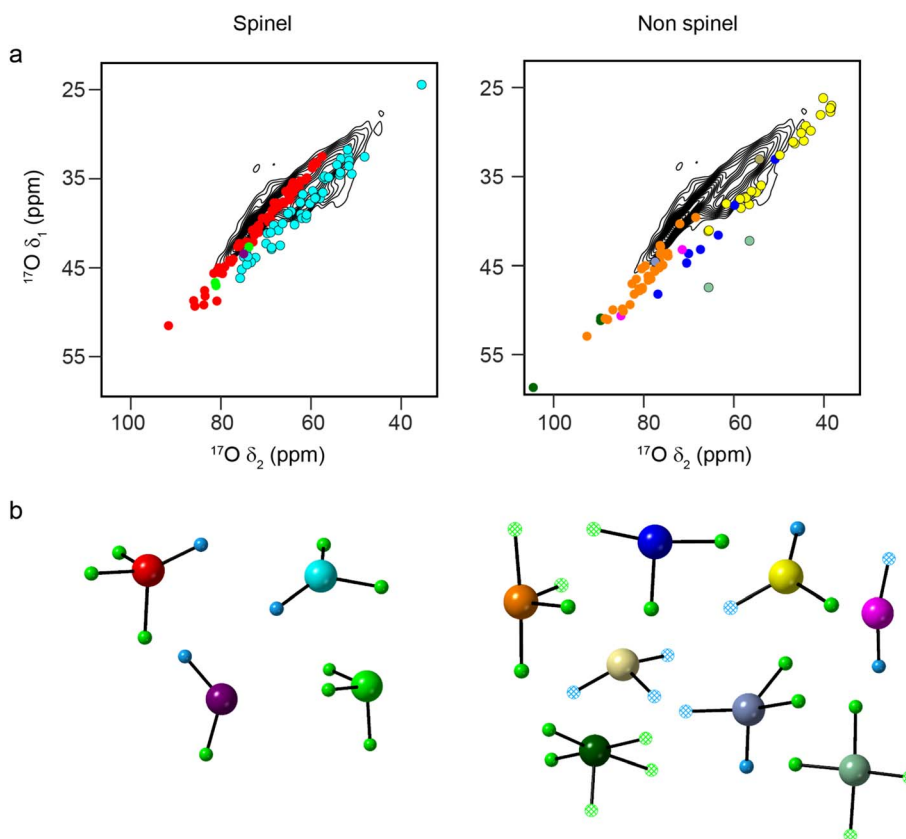


Fig. 3 (a) Plots showing the overlay of  $(\delta_1, \delta_2)$  centre-of-gravity shifts predicted (using DFT) for different O environments in  $3 \times 1 \times 1$  supercells of cubic and tetragonal non-spinel structural models of  $\gamma\text{-Al}_2\text{O}_3$  from Paglia,<sup>61</sup> with the  $^{17}\text{O}$  (20.0 T, 30 kHz) DQF-STMAS spectrum of  $\gamma\text{-Al}_2^{17}\text{O}_3$  (950  $^\circ\text{C}$ ) from Fig. 2b. The colours denote the local oxygen environments present (shown in (b)), which have been separated into “spinel” and “non-spinel”, as defined in the text. See the ESI† for the full structural models.



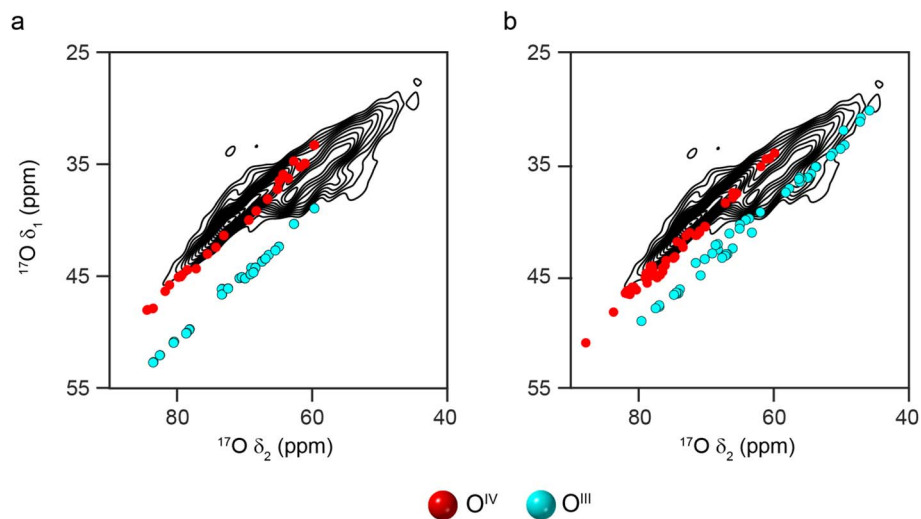


Fig. 4 Plots showing the overlay of  $(\delta_1, \delta_2)$  centre-of-gravity shifts predicted (using DFT) for different O environments in  $3 \times 1 \times 1$  supercells of cubic spinel structural models of  $\gamma\text{-Al}_2\text{O}_3$ , with the  $^{17}\text{O}$  (20.0 T, 30 kHz) DQF-STMAS spectrum of  $\gamma\text{-Al}_2^{17}\text{O}_3$  (950 °C) from Fig. 2b. In (a), vacancies appear only on  $\text{Al}^{\text{VI}}$  sites with maximum separation between them (see Model SP1 in the ESI†), while in (b), the distance between the vacancies is allowed to vary (see Model SP2 in the ESI†).

combination of experimental and computational evidence provided.

Fig. 2b shows the  $^{17}\text{O}$  STMAS spectrum of  $\gamma\text{-Al}_2\text{O}_3$  (950 °C), a sample enriched by heating in a 70%  $^{17}\text{O}_2$  atmosphere at 800 °C for 6 h and then increasing the temperature to 950 °C before heating for further 14 h (Fig. S2.1 in the ESI† shows a direct comparison of the  $^{17}\text{O}$  MAS NMR spectra of  $\gamma\text{-Al}_2\text{O}_3$  samples enriched at the two temperatures). The higher temperature leads to more efficient and more uniform enrichment (and

therefore higher sensitivity) but results in small impurities of  $\delta\text{-Al}_2\text{O}_3$  and  $\theta\text{-Al}_2\text{O}_3$ ,<sup>9,10</sup> as discussed in more detail in Section S2 of the ESI.† The spectrum shows two signals from the non-protonated O species – one centred at  $\delta_1$  of  $\sim 35$  ppm and a second centred at higher  $\delta_1$  ( $\sim 37.5$  ppm). Note that the signals from the protonated O species are not seen in the STMAS spectrum owing to very rapid relaxation (*vide infra*). To explore the likelihood of  $\text{Al}^{3+}$  cations occupying spinel or non-spinel environments, DFT calculations were used to predict  $^{17}\text{O}$

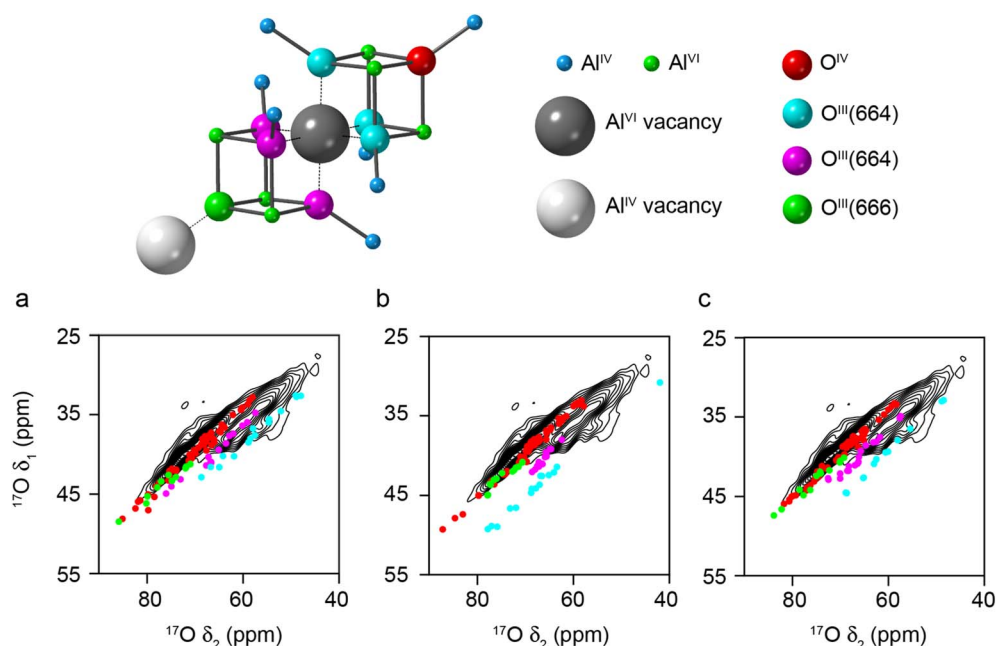
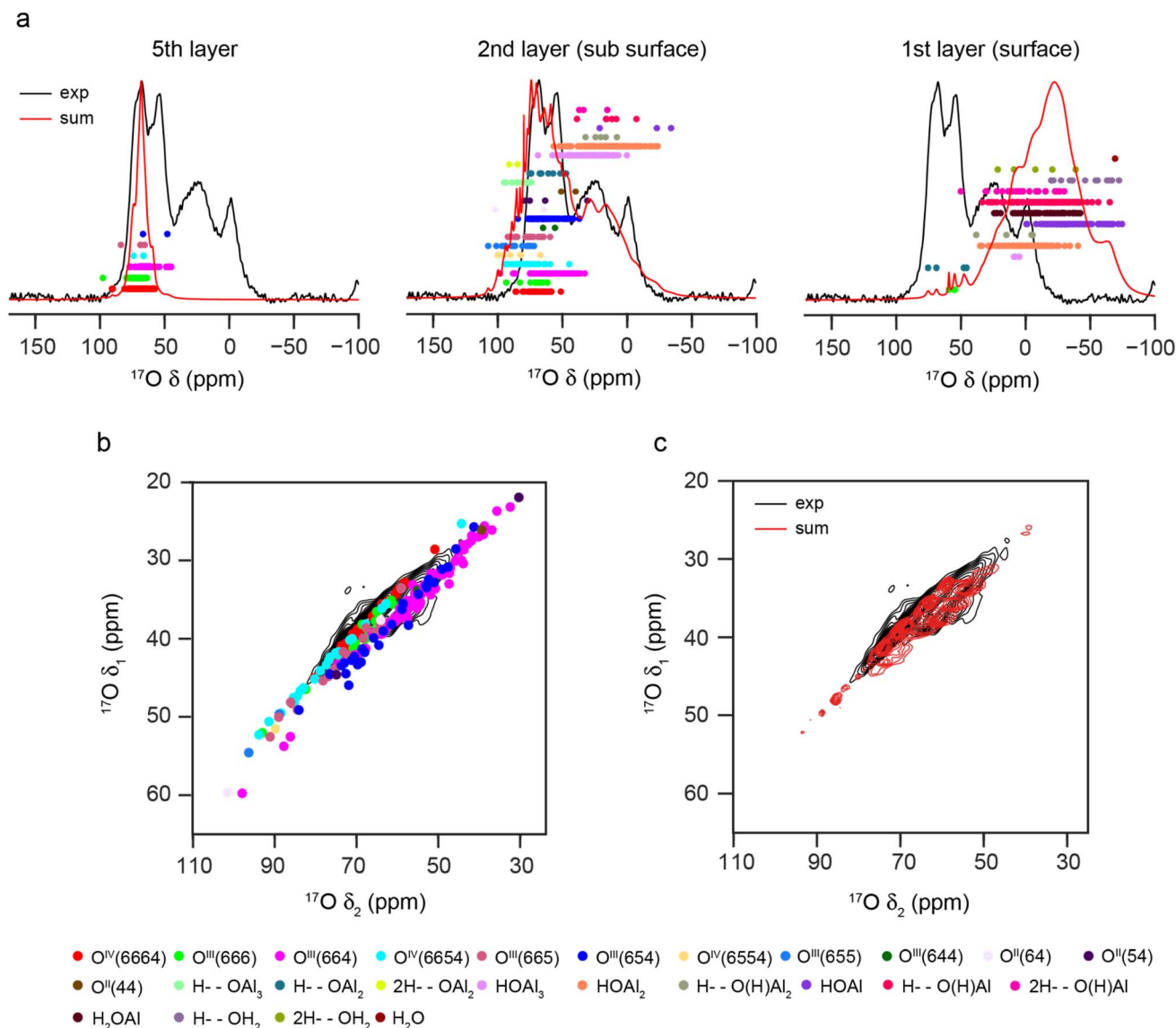


Fig. 5 Plots showing the overlay of  $(\delta_1, \delta_2)$  centre-of-gravity shifts predicted (using DFT) for different O environments in three different structural models (Models SP3-5, for (a), (b) and (c), respectively) generated from  $3 \times 1 \times 1$  supercells of cubic spinel structural models of  $\gamma\text{-Al}_2\text{O}_3$ , with the  $^{17}\text{O}$  (20.0 T, 30 kHz) DQF-STMAS spectrum of  $\gamma\text{-Al}_2^{17}\text{O}_3$  (950 °C) from Fig. 2b. In each structure, vacancies are present on  $\text{Al}^{\text{VI}}$  and  $\text{Al}^{\text{IV}}$  sites with maximum separation between them (see Fig. S3.4 of the ESI†). The key above shows the atom types and vacancies present.





**Fig. 6** (a) Plots showing the overlay of the DFT-predicted NMR shifts ( $\delta_2$ ) for all O in the slab models of  $\gamma\text{-Al}_2\text{O}_3$ , separated by the number of layers from the surface, with the  $^{17}\text{O}$  (20.0 T, 20 kHz) MAS NMR spectrum of  $\gamma\text{-Al}_2^{17}\text{O}_3$  (500 °C) from Fig. 2a. The red line results from co-adding Lorentzian lineshapes simulated for each O species, centred at the  $\delta_2$  centre-of-gravity with a FWHH proportional to  $C_Q$ . (b and c) Plots showing the overlay of ( $\delta_1$ ,  $\delta_2$ ) centre-of-gravity shifts predicted (using DFT) for non-protonated O environments in sub surface layer of the slab models of fully hydroxylated  $\gamma\text{-Al}_2\text{O}_3$ , with the  $^{17}\text{O}$  (20.0 T, 30 kHz) DQF-STMAS spectrum of  $\gamma\text{-Al}_2^{17}\text{O}_3$  (950 °C) from Fig. 2b. In (c), the red contours represent the spectrum simulated from the sum of Lorentzians for each of the points in (b), with a FWHH of 1.5 ppm in  $\delta_1$  and  $C_Q/\text{MHz ppm}$  in  $\delta_2$  the ESI.†

NMR parameters for two non-spinel structural models proposed by Paglia (using  $3 \times 1 \times 1$  supercells of the cubic and tetragonal unit cells).<sup>61</sup> Schematics of the structural models used are shown in Section S3 of the ESI.† As shown in Fig. 3a, the oxygen sites present can be divided into two types based on their first coordination sphere: “spinel” sites (*i.e.*, local environments that would occur in structures where all cations are restricted to spinel positions) and “non-spinel” sites (*i.e.*, local environments that can occur when this restriction is not in place). Fig. 3b overlays the predicted positions ( $\delta_1$ ,  $\delta_2$ ) of the centre-of-gravity of the signal from each O species on the experimental  $^{17}\text{O}$  STMAS spectrum of  $\gamma\text{-Al}_2^{17}\text{O}_3$  (950 °C) from Fig. 2b. The vast majority of the signals predicted for “non-spinel” species fall

outside of the regions where signal is observed experimentally, while the majority of the signals predicted for the “spinel” species are in much better agreement with the experiment, indicating that  $\gamma\text{-Al}_2^{17}\text{O}_3$  (950 °C) is unlikely to contain a high fraction of cations in non-spinel positions. It can also be seen that the signals from O<sup>III</sup>(644), shown in bright yellow (and also present in the low level  $\delta\text{-Al}_2\text{O}_3$  and  $\theta\text{-Al}_2\text{O}_3$  impurities<sup>9,10</sup>), overlay well with the shoulder seen on the STMAS lineshape, suggesting that this part of the signal may have a contribution from these impurities, as discussed in the ESI.† A second non-spinel model that is widely used for computational studies (as it contains only 14 atoms in the primitive unit cell) is that of Digne *et al.*,<sup>62</sup> which has three types of O environment (O<sup>IV</sup>(6664),



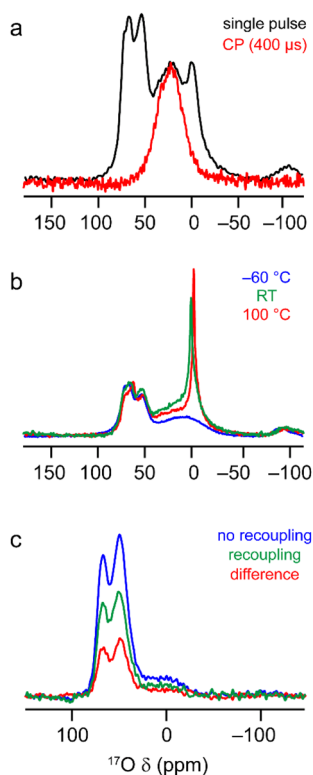


Fig. 7  $^{17}\text{O}$  MAS NMR of  $\gamma\text{-Al}_2\text{O}_3(500\text{ }^\circ\text{C})$ . (a) (20.0 T, 20 kHz) MAS and CP MAS NMR spectra acquired with  $\tau_{\text{CP}} = 400\ \mu\text{s}$ . (b) (20.0 T, 20 kHz) MAS NMR spectra acquired at varying temperatures. (c) (14.1 T, 14 kHz)  $^{17}\text{O}\text{-}^{27}\text{Al}$  TRAPDOR spectra acquired with  $\tau_{\text{rec}} = 16\ \tau_{\text{R}}$ . See Section S7 of the ESI† for more detailed experimental parameters and information on normalisation and scaling.

$\text{O}^{\text{IV}}(6666)$ , and  $\text{O}^{\text{III}}(664)$ , shown in Fig. 3 in red, orange and cyan, respectively).

Given the poor agreement with  $^{17}\text{O}$  NMR experiments for O species that can only occur in non-spinel models of  $\gamma\text{-Al}_2\text{O}_3$ , only

spinel models have been considered from this point forwards. Most previous computational studies on spinel-based models of  $\gamma\text{-Al}_2\text{O}_3$  have used the smallest unit cell that contains an integer number of vacancies (*i.e.*, a  $3 \times 1 \times 1$  supercell of the 14 atom primitive cell with two cation vacancies).<sup>11,14–20</sup> These suggested that lower energy structures were obtained when the cation vacancies were on the  $\text{Al}^{\text{VI}}$  sites and had the greatest separation between them. Here, we have used a larger model (a  $3 \times 1 \times 1$  supercell of the cubic spinel cell, with 160 atoms and eight cation vacancies). See the ESI† for more detail. Assuming the two requirements suggested above are retained, this model (Model SP1 in the ESI†) contains two types of O species;  $\text{O}^{\text{IV}}(6664)$  and  $\text{O}^{\text{III}}(664)$ . As shown in Fig. 4a, the DFT-predicted position of the  $^{17}\text{O}$  STMAS signals do not agree well with the experimental data. Although the points corresponding to  $\text{O}^{\text{IV}}$  (red) match reasonably well with the ridge centred at lower  $\delta_1$ , the  $\text{O}^{\text{III}}$  (cyan) points match poorly with the second ridge of signal (appearing at much higher ( $\delta_1$ ,  $\delta_2$ ) than seen in experiment), suggesting that at least one of the assumptions stated above is incorrect. If  $\text{Al}^{\text{VI}}$  vacancies are retained, but the requirement for maximum separation between them is not strictly enforced (see Model SP2 in the ESI†), the  $\text{O}^{\text{III}}$  signals predicted by DFT (see Fig. 4b) cover a much wider spectral range and overlap with some of the signal seen experimentally. The  $\text{O}^{\text{III}}(664)$  sites with lower  $\delta_{\text{iso}}$  values correspond to O species which are next to one  $\text{Al}^{\text{VI}}$  vacancy but are also close to a second. For O sites with  $\delta_2$  between 44 and 58 ppm, (corresponding to  $\delta_{\text{iso}}$  between 50–64 ppm) the next nearest vacancy is  $\sim 3.4\ \text{\AA}$  away, while for those with  $\delta_2 > 62\ \text{ppm}$  (corresponding to  $\delta_{\text{iso}} > 68\ \text{ppm}$ ), this distance is  $\sim 4.3\ \text{\AA}$ . This suggests that  $\gamma\text{-Al}_2\text{O}_3(950\text{ }^\circ\text{C})$  exhibits preferential clustering of the cation vacancies, contrary to the conclusions of previous computational studies.<sup>11,14–20</sup> However, the O sites present in the models used for the DFT calculations have slightly larger  $P_{\text{O}}$  values than those seen experimentally (and are more similar to the  $\text{O}^{\text{III}}(664)$  sites in  $\delta\text{-Al}_2\text{O}_3$  and  $\theta\text{-Al}_2\text{O}_3$ ).

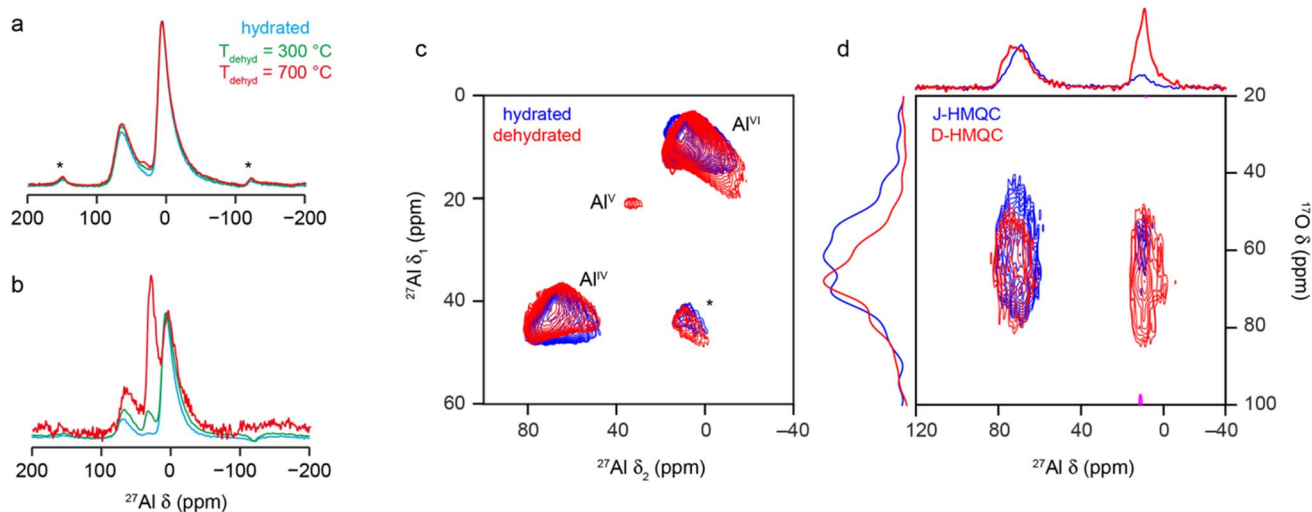


Fig. 8  $^{27}\text{Al}$  (9.4 T, 14 kHz) (a) MAS and (b) CP MAS NMR spectra of  $\gamma\text{-Al}_2\text{O}_3$ , hydrated (cyan) and dehydrated at  $300\text{ }^\circ\text{C}$  (green) and  $700\text{ }^\circ\text{C}$  (red). (c)  $^{27}\text{Al}$  (14.1 T, 14 kHz) MQ MAS spectrum of  $\gamma\text{-Al}_2\text{O}_3$  hydrated (blue) and dehydrated at  $300\text{ }^\circ\text{C}$  (red). (d)  $^{27}\text{Al}\text{-}^{17}\text{O}$  (20.0 T, 20 kHz) J-HMQC (blue) and D-HMQC (red) spectra of  $\gamma\text{-Al}_2\text{O}_3(950\text{ }^\circ\text{C})$ . For D-HMQC,  $\text{SR4}_2^1$  recoupling was applied for 0.9 ms. For detailed experimental parameters see Section S1 of the ESI.†



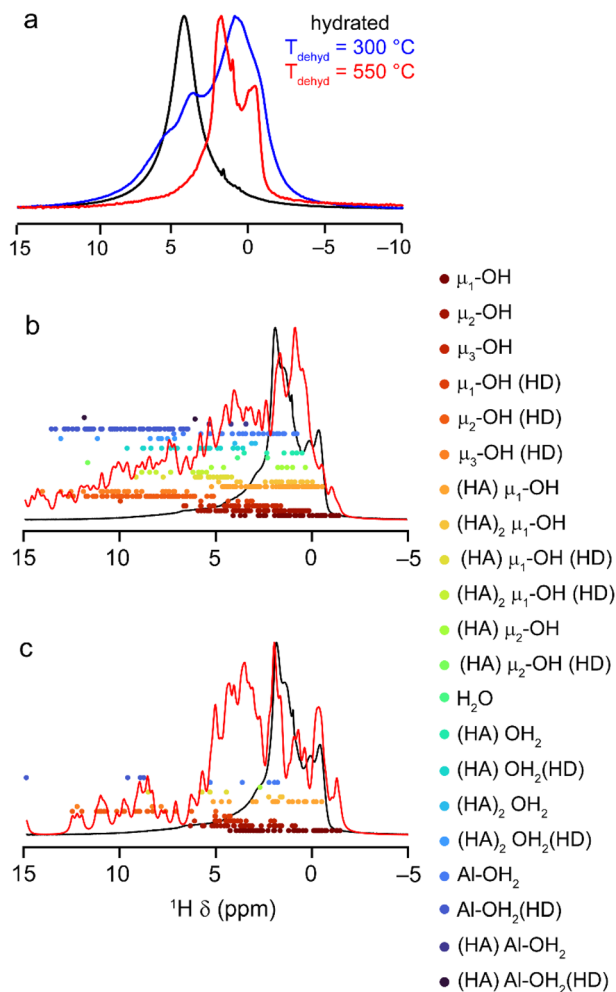


Fig. 9 (a)  $^1\text{H}$  (9.4 T, 14 kHz) DEPTH MAS NMR spectra of  $\gamma\text{-Al}_2\text{O}_3$  hydrated (black) and dehydrated at 300 °C (blue) and 550 °C (red). (b and c) Plots showing the overlay of the DFT-predicted NMR shifts ( $\delta_{\text{iso}}$ ) for all H in the (b) fully and (c) partially hydroxylated slab models of  $\gamma\text{-Al}_2\text{O}_3$ , overlaid with the  $^1\text{H}$  (14.1 T, 20 kHz) DEPTH MAS NMR spectrum of  $\gamma\text{-Al}_2\text{O}_3$  dehydrated at 550 °C. The red line represents the spectrum simulated from the sum of Lorentzians (FWHM of 150 Hz) added for each of the points shown. For detailed experimental parameters see the ESI.†

If the requirement for only  $\text{Al}^{\text{VI}}$  vacancies in the spinel model is also relaxed, and  $\text{Al}^{\text{IV}}$  vacancies are introduced, different O environments are then observed, as shown in Fig. 5 (see Models SP3-5 in the ESI.†). Fig. 5a-c show the DFT-predicted position of the  $^{17}\text{O}$  STMAS signals for the O species in three such models. The signals seen for a new O species,  $\text{O}^{\text{III}}(666)$ , shown in green, are very similar to the red points corresponding to  $\text{O}^{\text{IV}}(6664)$ , and in the  $^{17}\text{O}$  MAS spectrum would primarily contribute to the O signal at the highest  $\delta$  (previously assumed by Walter and Oldfield<sup>42</sup> to result only from  $\text{O}^{\text{IV}}$ ). It is also clear that  $\text{O}^{\text{III}}(664)$  signals fall into two distinct groups; those shown in cyan are very similar to those seen previously in Fig. 4 for structures where only  $\text{Al}^{\text{VI}}$  vacancies are present, and those shown in magenta, which have a smaller  $P_Q$  value ( $\sim 3$  MHz compared to  $\sim 4$  MHz) and are much closer to the values seen experimentally, matching well with the second ridge centred at higher  $\delta_1$ . The

difference between these two chemically similar species can be seen in Fig. 5, which shows that the second type of  $\text{O}^{\text{III}}(664)$  (magenta) is next to an  $\text{Al}^{\text{VI}}$  vacancy, and the next nearest  $\text{Al}^{\text{IV}}$  along the (110) planes is also missing. However, for the  $\text{O}^{\text{III}}(664)$  (cyan) this  $\text{Al}^{\text{IV}}$  is present. The  $\text{O}^{\text{III}}(664)$  magenta sites match much better with experimental measurements than the  $\text{O}^{\text{III}}(664)$  cyan sites, suggesting that it is likely that alternating  $\text{Al}^{\text{VI}}$  and  $\text{Al}^{\text{IV}}$  vacancies are present in  $\gamma\text{-Al}_2^{17}\text{O}_3(950\text{ °C})$ , and that there are roughly equal numbers of these.

Structural models with alternating  $\text{Al}^{\text{VI}}$  and  $\text{Al}^{\text{IV}}$  vacancies can be generated (see Models SP6-8 in the ESI.†). However, by definition, these must contain a line of  $\text{Al}^{\text{IV}}\text{-Al}^{\text{VI}}\text{-Al}^{\text{IV}}$  vacancies (see Fig. 5), although the next  $\text{Al}^{\text{VI}}$  vacancy can then be in the direction of any of the three neighbouring O atoms. In a real crystal this would generate complex vacancy “trajectories” and lead to many different O species in the resulting disordered solid. However, when limited to a 160 atom supercell this results in only a small number of possibilities and ordered structural models, leading to a relatively small number of distinct O species, which do not represent well the range that would appear in reality. The DFT-predicted  $^{17}\text{O}$  STMAS signals for these more ordered models are shown in Fig. S3.5 of the ESI.† The DFT calculations reproduce the experimental  $P_Q$  values well, but the  $\delta_{\text{iso}}$  values show a poorer match to experiment for the  $\text{O}^{\text{III}}(664)$  sites shown in magenta in Fig. 5, owing to the limited cell size and the ordered structures that result. In these models the  $\text{O}^{\text{III}}(664)$  species are either very close to, or very far from, a third Al vacancy (giving rise to very low or very high  $\delta_{\text{iso}}$  values, respectively). In a real material, a range of distances would be expected owing to the more disordered longer-range structure, leading to intermediate  $\delta_{\text{iso}}$  values in better agreement with experiment; however, this would require much more computationally costly calculations to explore in detail.

Although it is well known that the surface of  $\gamma\text{-Al}_2\text{O}_3$  is hydroxylated and hygroscopic, some studies have also suggested the presence of H in the bulk structure (from the boehmite precursor most commonly used in synthesis).<sup>63,64</sup> The only NMR spectroscopic study that supports this proposition was carried out a number of years ago using continuous wave (CW) NMR of static samples, and concluded that 37% of all protons are located in the bulk  $\gamma\text{-Al}_2\text{O}_3$ .<sup>65</sup> The more recent work of Paglia<sup>66</sup> did not report any evidence for significant levels of bulk H, a conclusion which is supported further by the fact that  $\gamma\text{-Al}_2\text{O}_3$  can also be produced from non-hydrogenous precursors.<sup>67</sup> To investigate the possibility of significant levels of  $^1\text{H}$  in the bulk structure of  $\gamma\text{-Al}_2\text{O}_3$ , DFT calculations were carried out for four further structural models (Models SPH1-4), generated as described in Section S4 of the ESI.† by replacing one  $\text{Al}^{3+}$  cation with three  $\text{H}^+$ . The DFT-predicted positions of the  $^{17}\text{O}$  STMAS signals are shown in Fig. S4.1 of the ESI.† The substitutions generate a new type of O species that acts as a hydrogen bond acceptor ( $\text{H-O}^{\text{III}}(664)$ ), which have similar NMR parameters to their non-hydrogen-bonded counterparts. No experimental  $^{17}\text{O}$  STMAS signals are seen for the protonated surface O species, owing to the rapid relaxation that results from dynamics between aluminols (*i.e.*,  $\text{Al-OH}$  species) and exchange with water (see later). However, such dynamics are likely to be



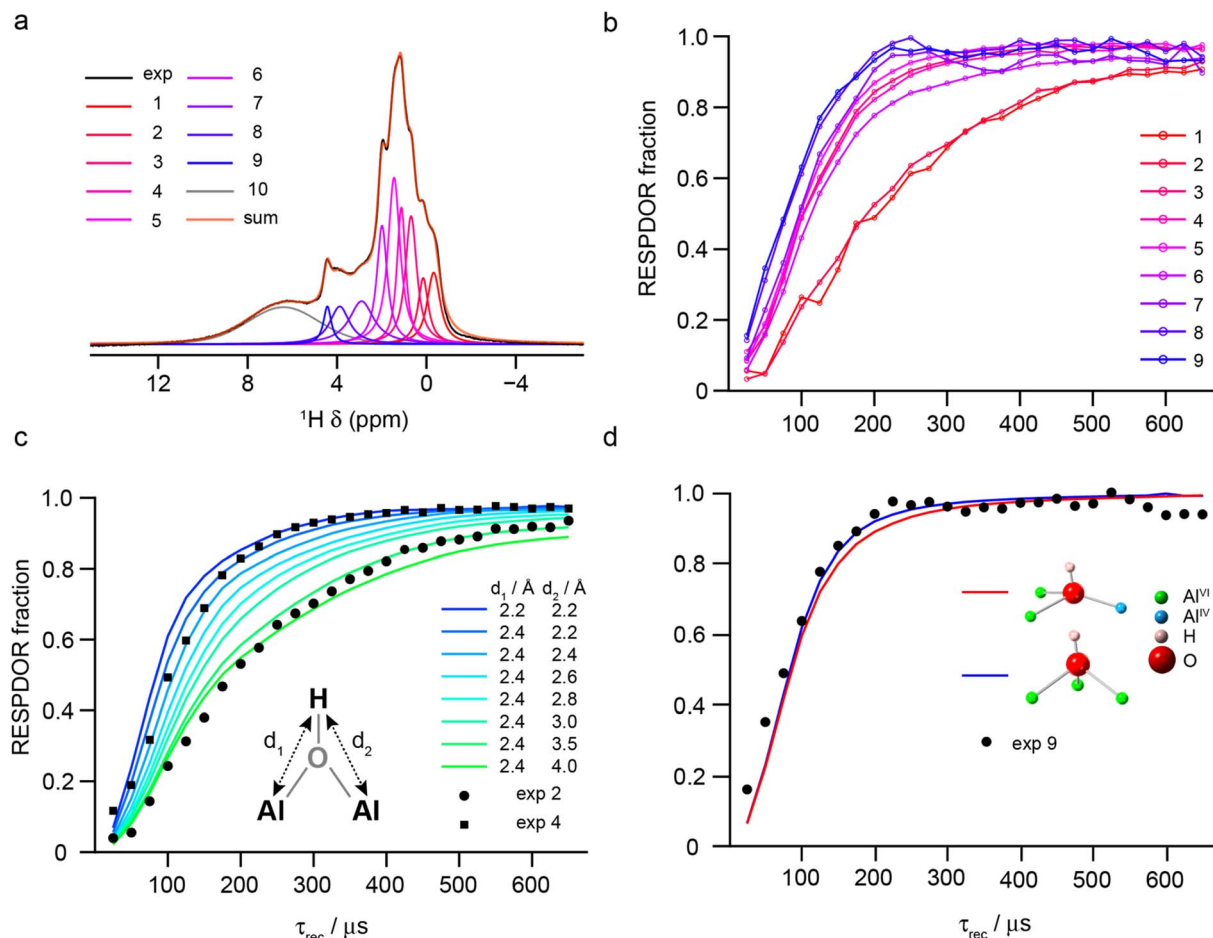


**Fig. 10** (a) Decomposition of the  $^1\text{H}$  (14.1 T, 40 kHz) DEPTH MAS NMR spectrum of  $\gamma\text{-Al}_2\text{O}_3$  dehydrated at 550  $^\circ\text{C}$  (blue) into the 10 components used in fits of the RESPDOR spectra. (b) Experimental RESPDOR curves (acquired using  $\text{R}12_3^5$  recoupling) plotted as a function of  $\tau_{\text{rec}}$ . (c) Overlay of experimental RESPDOR curves for components 2 and 4 with corresponding plots from numerical simulations of a three-spin ( $\text{H}_2\text{Al}$ ) system with varying H–Al distances, as shown. (d) Overlay of the experimental RESPDOR curve for component 9 with corresponding plots from numerical simulations of two four-spin ( $\text{H}_3\text{Al}$ ) systems for  $\mu_3$  aluminols extracted from the structural models above, as shown. In (c) and (d), the  $^{27}\text{Al}$   $C_Q$  was 5 MHz and in (c) the angle between the internuclear vectors was also fixed at 60 $^\circ$ . For detailed experimental parameters see Section S1 of the ESI $^\dagger$

much less pronounced for H in the bulk, and the corresponding protonated O species may be expected to appear in the  $^{17}\text{O}$  STMAS spectrum. Fig. S4.1 $^\dagger$  shows no evidence for these signals (also predicted to be at much lower  $\delta$ ) experimentally. There is also little evidence for the presence of bulk H in the experimental  $^1\text{H}$  DEPTH MAS NMR spectrum of dehydrated  $\gamma\text{-Al}_2\text{O}_3$  (550  $^\circ\text{C}$ ) shown in Fig. S4.2 of the ESI $^\dagger$  with no significant signal seen at the DFT-predicted  $\delta_{\text{iso}}$  values. In general, therefore, there is no evidence that  $\gamma\text{-Al}_2\text{O}_3$  contains a significant amount of H in the bulk structure.

Although it is generally accepted that the  $\text{O}^{2-}$  anions form an fcc array, the presence of stacking faults has been reported<sup>68</sup> and the presence of oxygen vacancies also proposed.<sup>69,70</sup> To investigate the latter, two further models of  $\gamma\text{-Al}_2\text{O}_3$  were considered, with the removal of 3  $\text{O}^{2-}$  and 2  $\text{Al}^{3+}$  cations from Model SP6. In Model SPV1 (see Section S5 of the ESI $^\dagger$ ) the O vacancies are more remote in the structure, whereas in Model SPV2 an “ $\text{Al}_2\text{O}_3$  unit” was removed with all of the vacancies clustered. In both cases, many new types of oxygen

environments are created that exhibit NMR parameters in poor agreement with the signals in  $^{17}\text{O}$  STMAS spectra (see Fig. S5.1 in the ESI $^\dagger$ ). This suggests that if such vacancies are present in bulk  $\gamma\text{-Al}_2\text{O}_3$ , they most likely occur only at very low levels.

The results discussed so far present an overall picture of bulk  $\gamma\text{-Al}_2\text{O}_3$  as having a fcc array of oxide ions with  $\text{Al}^{3+}$  occupying only spinel sites, with clusters and/or chains of Al vacancies on both  $\text{Al}^{\text{IV}}$  and  $\text{Al}^{\text{VI}}$  sites. The bulk appears to be anhydrous and there is little evidence of any significant disruption to the fcc array of O atoms (either stacking faults or clustered vacancies). While it is clear that  $\text{O}^{\text{IV}}$  and  $\text{O}^{\text{III}}$  species are present, our computational work suggests that these signals may overlap more than had been previously suggested (and the assignments used in previous work may be a simplification).

#### $^{17}\text{O}$ NMR spectroscopy: surface structure of $\text{Al}_2\text{O}_3$

Although there has been considerable debate over the structure of bulk  $\gamma\text{-Al}_2\text{O}_3$ , an understanding of the surface structure is more relevant from a catalysis perspective, and has been the



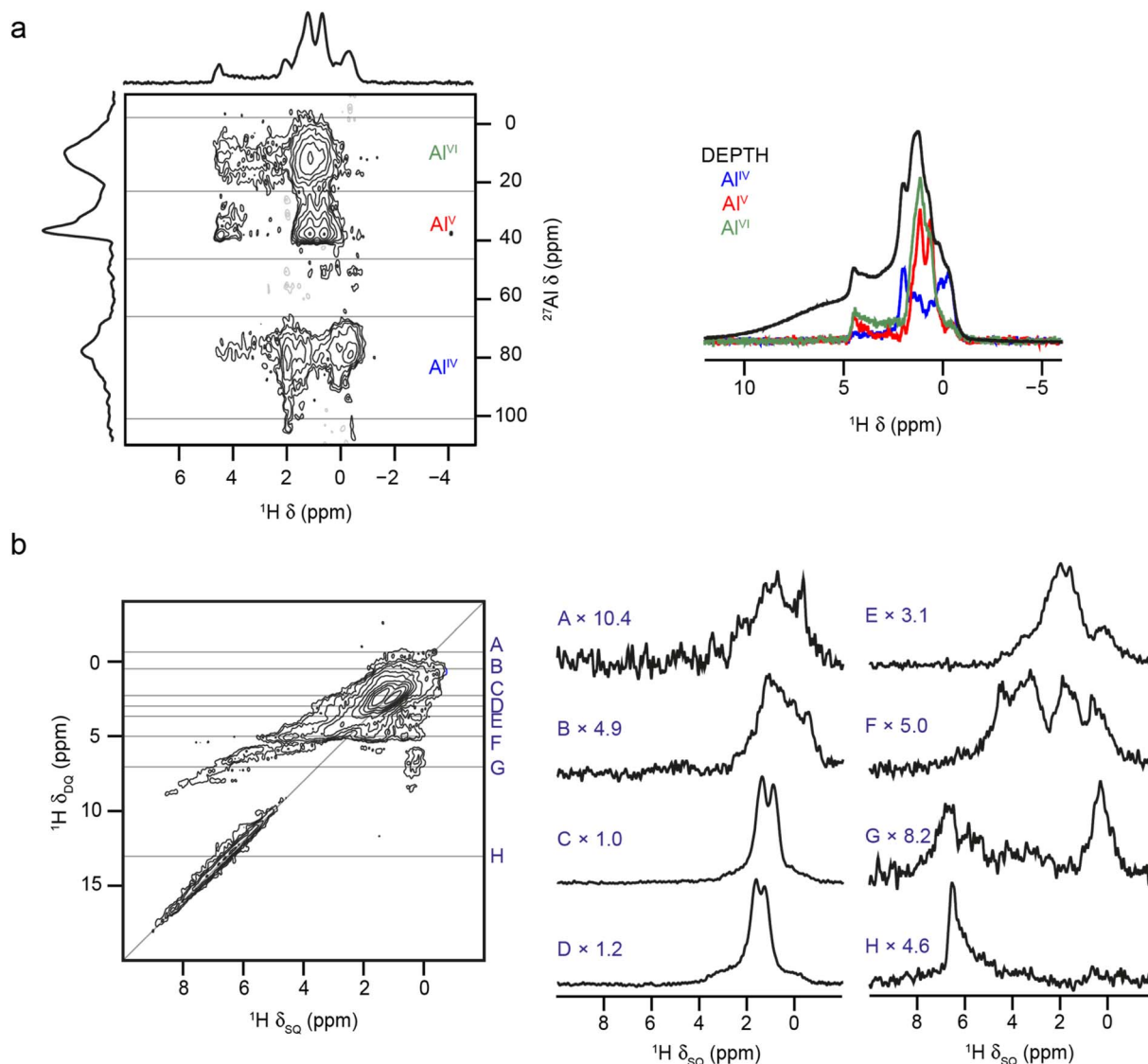


Fig. 11 (a)  $^1\text{H}$ - $^{27}\text{Al}$  (14.1 T, 40 kHz) D-HMQC spectrum (with TRAPDOR recoupling) of  $\gamma\text{-Al}_2\text{O}_3$  dehydrated at 550  $^\circ\text{C}$ , with sum projections (extracted parallel to  $\delta_2$ ) over the regions corresponding to Al<sup>IV</sup>, Al<sup>V</sup> and Al<sup>VI</sup> (as shown), overlaid with the  $^1\text{H}$  DEPTH (14.1 T, 40 kHz) DEPTH MAS NMR spectrum of  $\gamma\text{-Al}_2\text{O}_3$  dehydrated at 550  $^\circ\text{C}$ . (b)  $^1\text{H}$  (14.1 T, 40 kHz) DQ MAS spectrum (acquired using BABA recoupling) of  $\gamma\text{-Al}_2\text{O}_3$  dehydrated at 550  $^\circ\text{C}$ , with cross sections (extracted parallel to  $\delta_2$  and vertically expanded as shown) extracted at the  $\delta_1$  positions indicated. For detailed experimental parameters see Section S1 of the ESI.†

focus of much previous computational work.<sup>5,15,19,21,62,64</sup> The three surface planes of  $\gamma\text{-Al}_2\text{O}_3$ , (100), (110) and (111) as indexed in the cubic spinel unit cell,<sup>5</sup> are shown in Section S6 of the ESI,† where the surface arrangement of the  $\text{O}^{2-}$  anions and  $\text{Al}^{3+}$  cations are also highlighted. Unlike the (100) and (100) planes, normal to the (111) planes there are alternating layers of  $\text{O}^{2-}$  and  $\text{Al}^{3+}$  ions. Considering cation vacancies leads to a significantly larger number of inequivalent cleavages that could be performed. Structural models of “ $\gamma\text{-Al}_2\text{O}_3$  slabs” for DFT calculations were generated from the bulk models of  $\gamma\text{-Al}_2\text{O}_3$  by cleaving along the three surface planes as described in the ESI,† giving rise to 36 structural models (22 fully and 14 partially hydroxylated structures, each with two surfaces).

Fig. 6a overlays the  $^{17}\text{O}$  DFT-calculated  $\delta_2$  centre-of-gravity shifts (*i.e.*, including both  $\delta_{\text{iso}}$  and any second-order

quadrupolar shift) on the experimental  $^{17}\text{O}$  MAS NMR spectrum of  $\gamma\text{-Al}_2^{17}\text{O}_3$ (500  $^\circ\text{C}$ ). This is shown separately for oxygens in the surface layer, the sub surface layer and five layers from the surface. See Fig. S6.3 in the ESI† for the corresponding plots for O in layers three and four from the surface, and for plots of the ( $\delta_1$ ,  $\delta_2$ ) centre-of-gravity shifts for the non-protonated O in each of the five layers shown overlaid on the  $^{17}\text{O}$  STMAS spectrum of  $\gamma\text{-Al}_2^{17}\text{O}_3$ (950  $^\circ\text{C}$ ). For O species that are four and five oxide layers from the surface (not including any water layer), the NMR parameters are very similar to those calculated for O in the bulk models of  $\gamma\text{-Al}_2\text{O}_3$  discussed above, although the breaking of symmetry by the surface cleavage gives rise to a larger distribution of NMR parameters. The predicted shifts agree well with those seen experimentally. However, three layers from the surface (see Fig. S6.3 in the ESI†) a much greater number of



different types of non-protonated O species are seen (owing to the different coordination numbers of the neighbouring Al cations, many of which are now reduced by the cleavage). Three layers from the surface there is also an increasing number of O with lower  $\delta_{\text{iso}}$  (and  $\delta_2$ ) shifts, providing insight into the observation above that the most downfield resonance in the  $^{17}\text{O}$  MAS NMR spectrum increases in intensity when higher enrichment temperatures are used, enabling diffusion of  $^{17}\text{O}$  deeper into the material. In the sub surface layer, there is a large variety of protonated and non-protonated O environments present, which span the experimentally observed shift range. However, there are several points that fall outside of this range, notably for  $\text{O}^{\text{IV}}$ (6554) and  $\text{O}^{\text{III}}$ (655). These environments primarily occur in partially hydroxylated structures and so are not generally likely to be observed experimentally, where surfaces are fully hydroxylated and hydrated. Fig. 6b shows the overlay of the DFT-predicted ( $\delta_1$ ,  $\delta_2$ ) centre-of-gravity shifts for non-protonated O environments in the sub surface layers of the slab models of  $\gamma\text{-Al}_2\text{O}_3$ , with the  $^{17}\text{O}$  (20.0 T, 30 kHz) DQF-STMAS spectrum of  $\gamma\text{-Al}_2^{17}\text{O}_3$ (950 °C) from Fig. 2b. This shows relatively few points outside of the region where signals are observed experimentally, an observation which is perhaps illustrated more clearly in Fig. 6c, where Lorentzian lineshapes are applied to each of the points in Fig. 6b and summed. This result should not be interpreted as an indication that  $\gamma\text{-Al}_2^{17}\text{O}_3$ (950 °C) is enriched in  $^{17}\text{O}$  only as far as the sub surface layer but suggests that the variations in local geometry that arise from the presence of surfaces cannot be modelled well in the bulk models of  $\gamma\text{-Al}_2\text{O}_3$  used above.

The  $^{17}\text{O}$  MAS NMR spectrum of  $\gamma\text{-Al}_2^{17}\text{O}_3$ (500 °C) acquired at 20.0 T, shown in Fig. 7a, contains two signals from primarily protonated O species; a broad resonance at  $\sim 20$  ppm and a sharper signal at  $-2$  ppm (see Fig. S7.1 in the ESI† for results at 14.1 T). These signals have very short relaxation times ( $T_1$  of  $\sim 1.6$  and  $\sim 0.4$  ms, respectively, as measured by saturation recovery experiments, and  $T_2'$  of  $\sim 0.6$  and  $\sim 0.1$  ms, measured using rotor-synchronised single spin-echo experiments). This contrasts with the relaxation seen for the signals at higher shifts from non-protonated O ( $T_1$  of  $\sim 1\text{--}1.5$  s and  $T_2'$  of  $\sim 10$  ms), reflecting the involvement of the protonated O species in dynamic surface processes and their interactions with water. From Fig. 6a, the surface layers of the  $\gamma\text{-Al}_2\text{O}_3$  models contain only protonated O, with the majority of calculated  $\delta_2$  values lower than the signals seen experimentally. However, the  $\delta_2$  values for the protonated O in the sub surface layer match very well with the experimentally observed broader resonance, suggesting this results from less accessible O sites. The sharper resonance then likely results from averaging of the more accessible surface sites (which is also reflected in the faster  $T_1$  and  $T_2$  relaxation times for this signal). This is also supported by the observation that only the broader signal is seen in  $^1\text{H}\text{-}^{17}\text{O}$  cross polarisation (CP) spectra, as shown in Fig. 7a. Further evidence to support the assignment of the sharp signal at  $-2$  ppm to O in the surface layers is given in Fig. S7.2 in the ESI†, where it can be seen to vary in intensity with time and storage conditions. The  $^{17}\text{O}$  MAS NMR spectra of  $\gamma\text{-Al}_2^{17}\text{O}_3$ (500 °C) acquired at different temperatures, and shown in Fig. 7b,

reveal a significant change in linewidth of the sharp signal at lowest  $\delta_2$ , with broader lines seen at lower temperatures (suggesting dynamics are in the fast-intermediate regime). At  $-60$  °C, the sharp resonance becomes overlapped with the broader signal at higher  $\delta_2$ . Very little change is seen in the corresponding CP MAS NMR spectra, which still contain only the broader signal.

The computational results suggest that the broad signal for protonated O (at  $\sim 20$  ppm at 20.0 T) in the  $^{17}\text{O}$  MAS NMR spectrum arises primarily from aluminols (Al-OH species). However, there is an argument that this signal could, alternatively, be assigned to less mobile or strongly hydrogen bonded  $\text{H}_2^{17}\text{O}$  molecules. These species are likely to be much further from  $\text{Al}^{3+}$  cations and so the two types of signal could potentially be distinguished using  $^{17}\text{O}\text{-}^{27}\text{Al}$  dipolar dephasing measurements. Fig. 7c shows  $^{17}\text{O}\text{-}^{27}\text{Al}$  TRAPDOR<sup>71</sup> spectra of  $\gamma\text{-Al}_2^{17}\text{O}_3$ (500 °C), which demonstrate the presence of the broad signal from protonated O in the dephasing difference spectrum and confirm its assignment to aluminols. See the ESI† for a more detailed discussion of the recoupling experiments.

### $^{27}\text{Al}$ and $^1\text{H}$ NMR spectroscopy of $\text{Al}_2\text{O}_3$

As discussed briefly above, many of the previous spectroscopic studies of  $\gamma\text{-Al}_2\text{O}_3$  have focussed on  $^{27}\text{Al}$  NMR, which is sensitive to the Al coordination number (with  $\text{Al}^{\text{IV}}$ ,  $\text{Al}^{\text{V}}$  and  $\text{Al}^{\text{VI}}$  species found at  $\delta = 80$  to 50 ppm, 40 to 20 ppm and 20 to  $-20$  ppm, respectively, although exact shifts for a material are field dependent as  $I = 5/2$  for  $^{27}\text{Al}$ ). The  $^{27}\text{Al}$  MAS NMR spectrum (acquired with a short flip angle) of  $\gamma\text{-Al}_2\text{O}_3$  in Fig. 8a shows two broad signals, corresponding to  $\text{Al}^{\text{IV}}$  and  $\text{Al}^{\text{VI}}$ , in a *ca.* 1 : 2 ratio, with both exhibiting the tails to low frequency characteristic of disordered materials.<sup>39</sup> The  $^{27}\text{Al}$  MQMAS spectrum in Fig. 8c confirms distributions of both  $\delta_{\text{iso}}$  and  $P_{\text{Q}}$  are present (with average values as given in Section S8 of the ESI†).  $^{27}\text{Al}\text{-}^{17}\text{O}$  HMQC<sup>72</sup> experiments were performed both without (*i.e.*, J-HMQC) and with (D-HMQC) dipolar recoupling (using SR4<sub>1</sub><sup>73</sup>). For D-HMQC (as shown in Fig. 8d), all O signals correlate with  $\text{Al}^{\text{IV}}$  and  $\text{Al}^{\text{VI}}$  species as expected. However, for J-HMQC experiments the correlation is much stronger with  $\text{Al}^{\text{IV}}$  than with  $\text{Al}^{\text{VI}}$ . This somewhat surprising result may be understood by considering the values of the  $^{27}\text{Al}\text{-}^{17}\text{O}$   $J$  couplings for these two environments. These were calculated for Model SP6 of bulk  $\gamma\text{-Al}_2\text{O}_3$ , showing that  $\text{Al}^{\text{VI}}$  species have much smaller  $J$  couplings (*e.g.*,  $\sim 3\text{--}10$  Hz) than  $\text{Al}^{\text{IV}}$  (*e.g.*,  $\sim 7\text{--}20$  Hz), reflecting the higher ionicity (and consequently longer Al-O bonds) for  $\text{Al}^{\text{VI}}$ . See Section S9 of the ESI† for more detail. This would require longer HMQC evolution periods for efficient magnetisation transfer for  $\text{Al}^{\text{VI}}$ , although accessible values are ultimately limited by  $T_2$  (3–5 ms).

$\text{Al}^{\text{V}}$  species are not easily observed in the MAS or MQMAS spectra of hydrated bulk  $\gamma\text{-Al}_2\text{O}_3$ , although their low-level presence has been demonstrated previously.<sup>32,74–77</sup> Early studies<sup>32</sup> showed the concentration of  $\text{Al}^{\text{V}}$  depends on the exact synthetic route and conditions used, and particularly on any grinding of the precursor prior to calcination. Most studies indicate  $\text{Al}^{\text{V}}$  sites are preferentially, if not exclusively, located at



the surface. As discussed above, there is little evidence in the materials studied here for H in the bulk, and so  $^1\text{H}$ - $^{27}\text{Al}$  CP experiments can be used to selectively probe the alumina surface. For the hydrated  $\gamma\text{-Al}_2\text{O}_3$ , a low intensity  $\text{Al}^{\text{V}}$  signal can be seen between 20 and 40 ppm in the CP MAS spectrum in Fig. 8b. Dehydration will also affect the surface structure, increasing the relative intensity of  $\text{Al}^{\text{IV}}$  and  $\text{Al}^{\text{V}}$  species in the MAS and CP MAS NMR spectra (as shown in Fig. 8) with increasing dehydration temperature. Although not shown, the MAS spectrum does not change for samples dehydrated at 500 and 700 °C, suggesting the lower temperature is sufficient to remove the adsorbed water molecules. Dehydration yields a higher concentration of  $\text{Al}^{\text{V}}$  and their observation (albeit with very low intensity, at  $\delta_1 = 20$  ppm) in the  $^{27}\text{Al}$  MQMAS spectrum (as shown in Fig. 8c), with average NMR parameters as shown in Table S8.1 the ESI†

Early work using IR spectroscopy<sup>78</sup> suggested the presence of at least 5 different types of OH groups at the surface of  $\gamma\text{-Al}_2\text{O}_3$ . However, the  $^1\text{H}$  MAS NMR spectrum of hydrated  $\gamma\text{-Al}_2\text{O}_3$  is dominated by a broad resonance from water ( $\sim 4.5$  ppm) that obscures signals from surface aluminol groups, as shown in Fig. 9a. Upon dehydration, more complex spectral lineshapes are revealed. After dehydration at 300 °C, the lineshape is still relatively broad, but two distinct components (at  $\sim 3.7$  and 0.7 ppm) are resolved, with a shoulder at  $\sim 5.1$  ppm. When dehydration is carried out at a higher temperature (550 °C) a larger number of sharper signals are observed (with most between 0 and 4 ppm), although these are still significantly overlapped. The slow rehydration of the surface inside the NMR rotor (leading to increasing intensity at higher shifts) is shown in Fig. S10.1 in the ESI† It should be noted that no significant decrease in linewidth was observed with increasing MAS rate or with the application of homonuclear decoupling, suggesting that the linewidth results primarily from a distribution of chemical shifts.

The ranges of  $^1\text{H}$   $\delta_{\text{iso}}$  predicted using DFT for the 22 fully and 14 partially hydroxylated models of  $\gamma\text{-Al}_2\text{O}_3$  described above are shown in Fig. 9b and c, respectively. The  $^1\text{H}$  environments are grouped according to the denticity of the hydroxyl groups (with  $\mu_1$  being non bridging or terminal,  $\mu_2$  bridging and  $\mu_3$  a triply-bridged OH group), the coordination number of the  $\text{Al}^{3+}$  coordinated to the O, and whether the H is a hydrogen bond donor (HD) or the O a hydrogen bond acceptor (HA). The OH distance was considered a covalent bond when  $< 1.2$  Å. The spectra obtained from summing Lorentzians (FWHM of 150 Hz) of unit intensity applied to each data point do not match well with the experimental spectra in either case, but the range of shifts is reproduced well, and the spectra help in understanding the changes to the  $^1\text{H}$  MAS NMR spectrum seen with hydration. For a group of  $\mu_n$   $^1\text{H}$ , those H that act as hydrogen bond donors have higher shifts in each case. It is also noticeable that signals between 0 and 1 ppm result primarily from  $\mu_1$  and  $\mu_2$  hydrogen bond acceptor aluminols), in good agreement with the previous work of Deng and co-workers.<sup>43</sup> Similar plots considering predicted shifts for  $\mu_1$ ,  $\mu_2$  and  $\mu_3$  separately are given Fig. S10.2 in the ESI† (where the coordination numbers of the coordinated  $\text{Al}^{3+}$  are also denoted in each case). Comparison of these plots

confirms that the average  $^1\text{H}$  shift increases with denticity, negative shifts are only observed for non-bridging aluminols and that there is little dependence of the  $^1\text{H}$  shift on the coordination number of the  $\text{Al}^{3+}$  around O.

The denticity of the aluminol groups that produce different signals in the  $^1\text{H}$  MAS NMR spectrum was investigated experimentally using RESPDOR<sup>79</sup> to measure  $^1\text{H}$ - $^{27}\text{Al}$  dipolar couplings (see Section S1 of the ESI† for the experimental details). The  $^1\text{H}$  MAS NMR spectrum was decomposed into 10 separate Voigt components, nine of which were then used for analysis (see Section S10 of the ESI†), as shown in Fig. 10a. Fig. 10b shows the nine RESPDOR fractions ( $(S_0 - S)/S_0$ ) as a function of  $\tau_{\text{rec}}$ . Three groups of signals can be clearly distinguished, corresponding to components 1–2, 3–7 and 8–9. In Fig. 10c, the RESPDOR curves for components 2 and 4 are compared with numerical simulations for a  $^1\text{H}$ ( $^{27}\text{Al}$ )<sub>2</sub> spin system, with distances  $d_1$  and  $d_2$  determining the two different heteronuclear dipolar couplings. For all simulations, the  $^{27}\text{Al}$   $C_Q = 5$  MHz and the angle between the two internuclear vectors was fixed at 60°. Variation in these parameters has only a small effect on the RESPDOR fraction calculated (as shown in the ESI†). For component 2, a good match is obtained when  $d_1 < d_2$  (i.e., a  $\mu_1$  aluminol), which agrees with the DFT-predicted shift of these species. For component 4, simulation shows the best match is for  $d_1 = d_2 \approx 2.4$  Å, suggesting this group of signals result from  $\mu_2$  aluminols, which make up the most abundant H environments on the  $\gamma\text{-Al}_2\text{O}_3$  surface. Finally, as shown in Fig. 10d RESPDOR curves were simulated for the two most common types of  $\mu_3$  aluminols (spin system geometries were directly extracted from the structural models described above, with  $d_1$ ,  $d_2$  and  $d_3$  set to 2.4 Å). The simulation is in good agreement with the experimental result, confirming that components 8–9 ( $\delta_{\text{iso}} = 4\text{--}5$  ppm) can be attributed primarily to triply-bridging OH groups. These results agree with those of Taoufik *et al.*,<sup>77</sup> who were able to identify  $\mu_1$  and  $\mu_2$  aluminols, but also provides the assignment of signals from  $\mu_3$  aluminols, which have previously only been tentatively assigned based on their predicted higher shifts.

The coordination numbers of the Al cations attached to the aluminols were determined using  $^1\text{H}$ - $^{27}\text{Al}$  D-HMQC experiments (with TRAPDOR recoupling), as shown in Fig. 11a. Sum projections for shift regions corresponding to  $\text{Al}^{\text{IV}}$ ,  $\text{Al}^{\text{V}}$  and  $\text{Al}^{\text{VI}}$  show that  $\mu_1$  aluminols exhibit a weaker correlation with  $\text{Al}^{\text{V/VI}}$  than with  $\text{Al}^{\text{IV}}$  (a result consistent with previous work by Taoufik *et al.*<sup>77</sup> and Szeto *et al.*<sup>80</sup>). This reflects not only the higher abundance of  $\text{Al}^{\text{IV}}$  on partially dehydroxylated surfaces, but the increased difficulty of removing OH groups from these species (as opposed to  $\text{Al}^{\text{V}}$  and  $\text{Al}^{\text{VI}}$ ) species, as this would generate metastable  $\text{Al}^{\text{III}}$  environments. The existence of  $\text{Al}^{\text{III}}$  sites on alumina surfaces has been hypothesised in a range of previous work considering the reaction of  $\text{N}_2$ ,  $\text{H}_2$ ,  $\text{CH}_4$ , pyridine, CO and  $\text{CO}_2$  with alumina, and studied using computational approaches, NMR spectroscopy and IR spectroscopy.<sup>81–85</sup> The  $\text{Al}^{\text{III}}$  species are thought to result from high-temperature pretreatment of the surface (typically at  $\sim 700$  °C) and to be largely responsible for the adsorption of  $\text{N}_2$  or pyridine and the splitting of  $\text{CH}_4$  and  $\text{H}_2$ .<sup>82–85</sup> However, it has also been shown



that the level of water present plays an important role both in the changing the reactivity seen and in varying the coordination number of the Al species at the surface.<sup>81–83</sup> Direct detection of Al<sup>III</sup> species (if present) using NMR spectroscopy would be extremely challenging, owing the large quadrupolar couplings expected. In the current work, for  $\mu_2$  aluminols, coordination to all three types of Al is observed, but at higher  $\delta_{\text{H}}$  the correlation to Al<sup>V</sup> and Al<sup>VI</sup> is weaker, suggesting high levels of  $\mu_2$ -OH (Al-44), while the reverse is true at lower  $\delta_{\text{H}}$ , suggesting these <sup>1</sup>H signals result from species such as  $\mu_2$ -OH (Al-56) and  $\mu_2$ -OH (Al-66). For <sup>1</sup>H signals corresponding to  $\mu_3$  aluminols, correlations to Al<sup>IV</sup> are weaker, suggesting the most abundant species are  $\mu_3$ -OH (Al-666),  $\mu_3$ -OH (Al-665), *etc.* The spatial distribution of aluminols can be investigated using <sup>1</sup>H DQ MAS spectroscopy,<sup>86</sup> as in previous work.<sup>77</sup> Fig. 11b shows that  $\gamma$ -Al<sub>2</sub>O<sub>3</sub> dehydrated at 550 °C correlations between most types of aluminol <sup>1</sup>H are observed, although with differing intensities. This suggests no sites are exclusively isolated, but that the closest proximities are between bridging aluminols coordinated to Al<sup>IV</sup> and/or Al<sup>V</sup> species (traces C and D). This is perhaps not surprising given these are the most abundant species present on the surface, and these species also show correlations with all other types of <sup>1</sup>H (traces A, B, E and F). This observation can also be understood by considering the topology of the (100) and (110) surfaces (as shown in Fig. S6.1†). The (100) surface contains chains of Al<sup>V</sup> species which can, upon hydroxylation, accommodate neighbouring  $\mu_2$ -OH (Al-66) environments that do not share Al<sup>3+</sup> cations. At the (110) surface, chains of Al<sup>IV</sup> sites (generated from Al<sup>VI</sup>) are present, which can give rise to continuous chains of  $\mu_2$ -OH (Al-66) sharing Al<sup>VI</sup> cations, upon hydroxylation. This can also give rise to  $\mu_2$ -OH (Al-56) and  $\mu_2$ -OH (Al-55) at the ends of, or at breaks in, the chains. These topologies also explain the lower abundances of  $\mu_1$ -OH (Al-6) and  $\mu_1$ -OH (Al-5) relative to  $\mu_1$ -OH (Al-4). Upon hydroxylation of one such Al<sup>V</sup> or Al<sup>IV</sup> environment,  $\mu_1$ -OH (Al-6) or  $\mu_1$ -OH (Al-5) are formed, respectively, with two neighbouring coordinatively unsaturated aluminium sites. A small displacement of the oxygens of these hydroxyls generates a  $\mu_2$  aluminol, which is energetically more favourable. Chains of  $\mu_1$ -OH therefore give rise to corresponding chains of  $\mu_1$ -OH (Al-6) or  $\mu_1$ -OH (Al-5), which also do not correspond to the <sup>1</sup>H signals at lower  $\delta$ . Trace A shows autocorrelations between  $\mu_1$ -OH, while trace G demonstrates correlations between H that are hydrogen-bond donors and  $\mu_1$ -OH. The intensity of these cross peaks decreases significantly with recoupling time (see Fig. S10.4 of the ESI†), suggesting close proximity of the hydrogen-bond donors H and  $\mu_1$ -OH on the surface. Trace H confirms the autocorrelation of two hydrogen-bond donors (a signal which also decreases with recoupling time), suggesting this most likely arises from water. The only autocorrelation that is not observed is for  $\mu_3$ -OH, most likely because of their low overall concentration.

## Conclusions

In this work we have used a multinuclear NMR crystallographic approach, combining periodic planewave DFT calculations with experimental NMR spectroscopy of isotopically enriched

materials, to probe the detailed atomic-level structure of  $\gamma$ -Al<sub>2</sub>O<sub>3</sub>. Although each of these approaches has been used in previous work, the combination of all three in a single study here has demonstrated the complexity of the bulk material and range of surface species that may be present, and the challenge of unambiguously assigning (and quantifying) the experimental signals observed (an approach on which some previous literature conclusions have depended). This complexity has potentially limited prior analysis, and the insight obtained in this work provides new opportunities to interrogate this important system and related materials using NMR crystallography.

Comparison of experiment and computation suggested that the bulk structure of  $\gamma$ -Al<sub>2</sub>O<sub>3</sub> contained Al cations primarily in “spinel-like” sites, with roughly equal numbers of alternating Al<sup>VI</sup> and Al<sup>IV</sup> vacancies in disordered “chains” throughout. This contrasts with some previous work where Al vacancies were thought to occur exclusively on Al<sup>VI</sup> sites, with a maximum separation between them. The use of a larger unit cell for the calculations enabled a wide range of local environments to be generated, and the inclusion of Al<sup>IV</sup> vacancies produces many new types of <sup>17</sup>O signals, and notably O<sup>III</sup> sites with very similar parameters to O<sup>IV</sup> signals. This highlights potential problems with previous work, where many conclusions relied on an unambiguous assignment (and quantification) of O<sup>III</sup> and O<sup>IV</sup> signals and correlations of these with other species to determine local structure. There was no evidence for the presence of H in the bulk structure of  $\gamma$ -Al<sub>2</sub>O<sub>3</sub>, or for any significant levels of O vacancies.

While catalysis is often a surface phenomenon, the surface structure is inherently related to the position, type and ordering of Al vacancies found in the bulk. Applying an NMR crystallographic approach to three separate surfaces made from a set of our structural models with different cation vacancies and different levels of hydration, enabled the prediction of <sup>17</sup>O NMR spectra for surface, sub surface and bulk species. This showed that even at the third oxide layer from the surface many different types of O species are formed owing to the different coordination numbers of the neighbouring Al cations, many of which are now reduced by the cleavage, providing additional support for the assignment and interpretation of the complex resonances in the <sup>17</sup>O NMR spectra.

Relaxation measurements highlighted the involvement of protonated O species in dynamic surface processes and their interactions with water, with the rapid relaxation seen accounting for the absence of these signals in STMAS (and MQMAS) spectra. Through VT, CP and TRAPDOR experiments, and by comparison to DFT calculations, it was possible to assign the two signals seen, with the sharper and broader resonances attributed to more accessible surface sites that often interact strongly with water and less accessible aluminols, respectively. <sup>17</sup>O-<sup>27</sup>Al D-HMQC spectra showed that all O signals correlate to Al<sup>IV</sup> and Al<sup>VI</sup> species but, somewhat surprisingly, J-HMQC experiments suggested that the correlations are much stronger with Al<sup>IV</sup> than with Al<sup>VI</sup>. However, this is likely to result from the different *J* couplings, with O–Al<sup>VI</sup> couplings much smaller (3–10 Hz) than O–Al<sup>IV</sup> couplings, reflecting the different



bond lengths, rather than a difference in the presence of these atom pairs.

DFT-predicted  $^1\text{H}$  NMR parameters confirmed the  $^1\text{H}$  shift generally increases with denticity (in agreement with previous work), and that, although a wide range of shifts are seen depending on the coordinated atoms, there is little direct dependence of the  $^1\text{H}$  shift on the Al coordination number. Spectral assignments were also supported by  $^1\text{H}$ - $^{27}\text{Al}$  RESPDOR experiments, which identified spectral components resulting from  $\mu_1$ ,  $\mu_2$  and  $\mu_3$  aluminols. Combining these with  $^1\text{H}$ - $^{27}\text{Al}$  D-HMQC experiments showed that (i)  $\mu_1$  aluminols are more likely to be bound to  $\text{Al}^{\text{IV}}$ , (ii)  $\mu_2$  aluminols are coordinated to all three types of Al, e.g.,  $\mu_2$ -OH (Al-44),  $\mu_2$ -OH (Al-56) and  $\mu_2$ -OH (Al-66) and (iii)  $\mu_3$  aluminols are most likely bound to higher coordinated Al species, e.g.,  $\mu_3$ -OH (Al-666) and  $\mu_3$ -OH (Al-665). DQ MAS spectroscopy confirmed no types of aluminols exist exclusively in isolation but showed that the closest proximities are between bridging aluminols coordinated to  $\text{Al}^{\text{IV}}$  and/or  $\text{Al}^{\text{V}}$  species, reflecting the likely topology of the surfaces.

The combination of multinuclear NMR spectroscopy with both isotopic enrichment and DFT calculations has provided more detailed insight into both the bulk and surface structure of  $\gamma$ - $\text{Al}_2\text{O}_3$ . The complexity of both bulk and surface structures that this reveals highlights the challenges faced by any study, and the need to combine approaches to obtain a much fuller picture. The different results observed in this work from some previous studies may reflect the natural advances in both computation and experiment over the years but are also likely to result from the varied nature of aluminas depending on the route by which they are synthesised and how they have been treated or stored. While this adds to the challenge of control for catalytic applications, it also offers an exceptional opportunity to fine tune the properties of the surfaces and their modification if the detailed atomic-level structure of these materials can be understood. The insight achieved here will provide a basis for future work both on the reactivity of aluminas themselves and on their modified surfaces.

## Data availability

Detailed experimental parameters, structural models used for DFT calculations, further  $^{17}\text{O}$ ,  $^{27}\text{Al}$  and  $^1\text{H}$  NMR spectra and calculated  $^{27}\text{Al}$ - $^{17}\text{O}$   $J$  couplings are given in the ESI.† The research data (and/or materials) supporting this publication can be accessed at <https://doi.org/10.17630/5020123c-d803-4bfd-8228-3e2507f077e4>.<sup>87</sup> In order to meet institutional and research funder open access requirements, any accepted manuscript arising shall be open access under a Creative Commons Attribution (CC BY) reuse licence with zero embargo.

## Author contributions

SEA and PBW co-conceived and funded the project and had oversight and supervision of the work. MLB carried out the experimental and computational work. DMD supported the acquisition, analysis and curation of the NMR data and

contributed to the preparation of the figures. SEA wrote the initial manuscript and all authors contributed to the final draft.

## Conflicts of interest

There are no conflicts of interest to declare.

## Acknowledgements

The authors would like to thank Sasol for partial funding of a studentship for MBL, and EPSRC for support through the Collaborative Computational Project on NMR Crystallography (CCP-NC), *via* EP/M022501/1 and EP/T026642/1. PBW also thanks the Royal Society for the award of a Royal Society Industry Fellowship. The authors would like to thank Dr Andrew Rankin for help with preliminary experiments. The UK High-Field Solid-State NMR Facility used in this research was funded by EPSRC and BBSRC (EP/T015063/1) as well as the University of Warwick including *via* part funding through Birmingham Science City Advanced Materials Projects 1 and 2 supported by Advantage West Midlands (AWM) and the European Regional Development Fund (ERDF). Collaborative assistance from the Facility Manager Team (Dinu Iuga, University of Warwick) is acknowledged.

## References

- 1 M. Trueba and S. P. Trasatti, *Eur. J. Inorg. Chem.*, 2005, 3393–3403.
- 2 G. Busca, *Chem. Rev.*, 2007, **107**, 5366–5410.
- 3 *Fischer-Tropsch Technology*, ed. A. P. Steynberg and M. E. Dry, Elsevier, 1st edn, 2004.
- 4 W. H. Shearon and W. R. Fullem, *Ind. Eng. Chem.*, 1959, **51**, 720–726.
- 5 G. Busca, *Catal. Today*, 2014, **226**, 2–13.
- 6 G. Busca, *Catal. Today*, 2020, **357**, 621–629.
- 7 K. Wefers and C. Misra, *Alcoa Tech. Pap.*, 1987, **19**, 1–100.
- 8 I. Levin and K. C. Brandon, *J. Am. Ceram. Soc.*, 2005, **81**, 1995–2012.
- 9 L. Kovarik, M. Bowden, A. Genc, J. Szanyi, C. H. F. Peden and J. H. Kwak, *J. Phys. Chem. C*, 2014, **118**, 18051–18058.
- 10 L. Kovarik, M. Bowden, D. Shi, N. M. Washton, A. Andersen, J. Z. Hu, J. Lee, J. Szanyi, J. H. Kwak and C. H. F. Peden, *Chem. Mater.*, 2015, **27**, 7042–7049.
- 11 C. Wolverton and K. C. Hass, *Phys. Rev. B: Condens. Matter Mater. Phys.*, 2000, **63**, 024102.
- 12 E. J. W. Verwey, *Z. Kristallogr. Cryst. Mater.*, 1935, **91**, 65–69.
- 13 B. C. Lippens and J. H. de Boer, *Acta Cryst.*, 1964, **17**, 1312–1321.
- 14 S.-D. Mo, Y.-N. Xu and W.-Y. Ching, *J. Am. Ceram. Soc.*, 2005, **80**, 1193–1197.
- 15 C. Y. Ouyang, Ž. Šljivančanin and A. Baldereschi, *Phys. Rev. B: Condens. Matter Mater. Phys.*, 2009, **79**, 235410.
- 16 F. H. Streitz and J. W. Mintmire, *Phys. Rev. B: Condens. Matter Mater. Phys.*, 1999, **60**, 773–777.
- 17 G. Gutiérrez, A. Taga and B. Johansson, *Phys. Rev. B: Condens. Matter Mater. Phys.*, 2001, **65**, 012101.



- 18 A. Vijay, G. Mills and H. Metiu, *J. Chem. Phys.*, 2002, **117**, 4509–4516.
- 19 H. P. Pinto, R. M. Nieminen and S. D. Elliott, *Phys. Rev. B: Condens. Matter Mater. Phys.*, 2004, **70**, 125402.
- 20 E. Menéndez-Proupin and G. Gutiérrez, *Phys. Rev. B: Condens. Matter Mater. Phys.*, 2005, **72**, 035116.
- 21 S. Blonski and S. H. Garofalini, *Surf. Sci.*, 1993, **295**, 263–274.
- 22 M.-H. Lee, C.-F. Cheng, V. Heine and J. Klinowski, *Chem. Phys. Lett.*, 1997, **265**, 673–676.
- 23 K. P. Sinha and A. P. B. Sinha, *J. Phys. Chem.*, 1957, **61**, 758–761.
- 24 J. A. Wang, X. Bokhimi, A. Morales, O. Novaro, T. López and R. Gómez, *J. Phys. Chem. B*, 1999, **103**, 299–303.
- 25 Y. G. Wang, P. M. Bronsveld, J. T. M. DeHosson, B. Djuričić, D. McGarry and S. Pickering, *J. Am. Ceram. Soc.*, 2005, **81**, 1655–1660.
- 26 G. Kryukova, D. Klenov, A. Ivanova and S. Tsybulya, *J. Eur. Ceram. Soc.*, 2000, **20**, 1187–1189.
- 27 B. Ealet, M. H. Elyakhloufi, E. Gillet and M. Ricci, *Thin Solid Films*, 1994, **250**, 92–100.
- 28 R. Dupree, M. H. Lewis and M. E. Smith, *Philos. Mag. A*, 1986, **53**, L17–L20.
- 29 H. Saalfeld, *Clay Miner.*, 1958, **3**, 249–257.
- 30 V. Jayaram and C. G. Levi, *Acta Metall.*, 1989, **37**, 569–578.
- 31 C. Pecharrmán, I. Sobrados, J. E. Iglesias, T. González-Carreño and J. Sanz, *J. Phys. Chem. B*, 1999, **103**, 6160–6170.
- 32 F. Chen, J. G. Davis and J. J. Fripiat, *J. Catal.*, 1992, **133**, 263–278.
- 33 D. Iuga, *J. Magn. Reson.*, 2011, **208**, 225–234.
- 34 G. Paglia, C. E. Buckley, A. L. Rohl, R. D. Hart, K. Winter, A. J. Studer, B. A. Hunter and J. V. Hanna, *Chem. Mater.*, 2004, **16**, 220–236.
- 35 G. Paglia, C. E. Buckley, A. L. Rohl, B. A. Hunter, R. D. Hart, J. V. Hanna and L. T. Byrne, *Phys. Rev. B: Condens. Matter Mater. Phys.*, 2003, **68**, 144110.
- 36 V. A. Ushakov and E. M. Moroz, *React. Kinet. Catal. Lett.*, 1984, **24**, 113–118.
- 37 R.-S. Zhou and R. L. Snyder, *Acta Crystallogr., Sect. B: Struct. Sci.*, 1991, **47**, 617–630.
- 38 X. Krokidis, P. Raybaud, A.-E. Gobichon, B. Rebours, P. Euzen and H. Toulhoat, *J. Phys. Chem. B*, 2001, **105**, 5121–5130.
- 39 R. F. Moran, D. M. Dawson and S. E. Ashbrook, *Int. Rev. Phys. Chem.*, 2017, **36**, 39–115.
- 40 P. Euzen, P. Raybaud, X. Krokidis, H. Toulhoat, J.-L. Le Loarer, J.-P. Jolivet and C. Froidefond, in *Handbook of Porous Materials*, ed. F. Schüth, K. Sing and J. Weitkamp, Wiley-VCH, Weinheim, Germany, 2002, ch. 4.7.2, pp 1591–1677.
- 41 S. E. Ashbrook and M. E. Smith, *Chem. Soc. Rev.*, 2006, **35**, 718–735.
- 42 T. H. Walter and E. Oldfield, *J. Phys. Chem.*, 1989, **93**, 6744–6751.
- 43 Q. Wang, W. Li, I. Hung, F. Mentink-Vigier, X. Wang, G. Qi, X. Wang, Z. Gan, J. Xu and F. Deng, *Nat. Commun.*, 2020, **11**, 3620.
- 44 W. Li, Q. Wang, J. Xu, F. Aussenac, G. Qi, X. Zhao, P. Gao, C. Wang and F. Deng, *Phys. Chem. Chem. Phys.*, 2018, **20**, 17218–17225.
- 45 L. Shen, Y. Wang, J. Du, K. Chen, Z. Lin, Y. Wen, I. Hung, Z. Gan and L. Peng, *ChemCatChem*, 2020, **12**, 1569–1574.
- 46 R. Prins, *Angew. Chem., Int. Ed.*, 2019, **58**, 15548–15552.
- 47 H. Nagashima, J. Trebosc, O. Lafon and J.-P. Amoureux, *J. Magn. Reson. Open*, 2024, **21**, 100177.
- 48 L. Frydman and J. S. Harwood, *J. Am. Chem. Soc.*, 1995, **117**, 5367–5368.
- 49 H. T. Kwak and Z. Gan, *J. Magn. Reson.*, 2003, **164**, 369–372.
- 50 S. E. Ashbrook and S. Wimperis, *Prog. Nucl. Magn. Reson. Spectrosc.*, 2004, **45**, 53–108.
- 51 C. J. Pickard and F. Mauri, *Phys. Rev. B: Condens. Matter Mater. Phys.*, 2001, **63**, 245101.
- 52 S. J. Clark, M. D. Segall, C. J. Pickard, P. J. Hasnip, M. J. Probert, K. Refson and M. C. Payne, *Z. Kristallogr. Cryst. Mater.*, 2005, **220**, 567–570.
- 53 S. A. Joyce, J. R. Yates, C. J. Pickard and F. Mauri, *J. Chem. Phys.*, 2007, **127**, 204107.
- 54 J. P. Perdew, K. Burke and M. Ernzerhof, *Phys. Rev. Lett.*, 1996, **77**, 1865–1868.
- 55 A. Tkatchenko and M. Scheffler, *Phys. Rev. Lett.*, 2009, **102**, 073005.
- 56 J. R. Yates, C. J. Pickard, M. C. Payne and F. Mauri, *J. Chem. Phys.*, 2003, **118**, 5746–5743.
- 57 H. J. Monkhorst and J. D. Pack, *Phys. Rev. B: Condens. Matter Mater. Phys.*, 1976, **13**, 5188–5192.
- 58 H. J. Jakobsen, J. Skibsted, H. Blidsoe and N. C. Nielsen, *J. Magn. Reson.*, 1989, **85**, 173–180.
- 59 P. Pykkö, *Mol. Phys.*, 2018, **116**, 1328–1338.
- 60 M. Bak, J. T. Rasmussen and N. C. Nielsen, *J. Magn. Reson.*, 2000, **147**, 296–330.
- 61 G. Paglia, Determination of the Structure of  $\gamma$ -Alumina using Empirical and First-Principles Calculations Combined with Supporting Experiments, PhD thesis, Curtin University of Technology, 2004.
- 62 M. Digne, P. Sautet, P. Raybaud, P. Euzen and H. Toulhoat, *J. Catal.*, 2004, **226**, 54–68.
- 63 D. A. Dowden, *J. Chem. Soc.*, 1950, 242–265.
- 64 K. Sohlberg, S. J. Pennycook and S. T. Pantelides, *Chem. Eng. Commun.*, 2000, **181**, 107–135.
- 65 R. Pearson, *J. Catal.*, 1971, **23**, 388–394.
- 66 G. Paglia, C. E. Buckley, T. J. Udovic, A. L. Rohl, F. Jones, C. F. Maitland and J. Connolly, *Chem. Mater.*, 2004, **16**, 1914–1923.
- 67 L. Smrcek, V. Langer and J. Krestan, *Acta Crystallogr. Sect. C Cryst. Struct. Commun.*, 2006, **62**, 83–84.
- 68 G. Paglia, E. S. Božin and S. J. L. Billinge, *Chem. Mater.*, 2006, **18**, 3242–3248.
- 69 S. K. Sharma, P. Das and B. K. Sanfui, *Mol. Syst. Des. Eng.*, 2022, **7**, 67–91.
- 70 M. E. Miller and S. T. Mixture, *J. Phys. Chem. C*, 2010, **114**, 13039–13046.
- 71 C. P. Grey and A. J. Vega, *J. Am. Chem. Soc.*, 1995, **117**, 8232–8242.



- 72 A. Lesage, D. Sakellariou, S. Steuernagel and L. Emsley, *J. Am. Chem. Soc.*, 1998, **120**, 13194.
- 73 A. Brinkmann and A. P. M. Kentgens, *J. Am. Chem. Soc.*, 2006, **128**, 14758–14759.
- 74 R. Wischert, P. Florian, C. Copéret, D. Massiot and P. Sautet, *J. Phys. Chem. C*, 2014, **118**, 15292–15299.
- 75 J. H. Kwak, J. Hu, A. Lukaski, D. H. Kim, J. Szanyi and C. H. F. Peden, *J. Phys. Chem. C*, 2008, **112**, 9486–9492.
- 76 J. H. Kwak, J. Hu, D. Mei, C. -W. Yi, D. H. Kim, C. H. F. Peden, L. F. Allard and J. Szanyi, *Science*, 2009, **325**, 1670–1673.
- 77 M. Taoufik, K. C. Szeto, N. Merle, I. Del Rosal, L. Maron, J. Trébosc, G. Tricot, R. M. Gauvin and L. H. Delevoye, *Chem.–Eur. J.*, 2014, **20**, 4038–4046.
- 78 H. Knözinger and P. Ratnasamy, *Catal. Rev.*, 1978, **17**, 31–70.
- 79 L. Chen, Q. Wang, B. Hu, O. Lafon, J. Trébosc, F. Deng and J. P. Amoureux, *Phys. Chem. Chem. Phys.*, 2010, **12**, 9395–9405.
- 80 K. C. Szeto, N. Merle, J. Trébosc, M. Taoufik, R. M. Gauvin, F. Pourpoint and L. Delevoye, *J. Phys. Chem. C*, 2019, **123**, 12919–12927.
- 81 V. Sanchez Escribano, G. Garbarino, E. Finocchio and G. Busca, *Top. Catal.*, 2017, **60**, 1554–1564.
- 82 R. Wishert, P. Laurent, C. Coperet, F. Delbecq and P. Sautet, *J. Am. Chem. Soc.*, 2012, **134**, 14430–14449.
- 83 R. Wishert, C. Coperet, F. Delbecq and P. Sautet, *Angew. Chem.*, 2011, **50**, 3202–3205.
- 84 J. Joubert, A. Salameh, V. Krakoviack, F. Delbecq, P. Sautet, C. Coperet and J.-M. Basset, *J. Phys. Chem. B*, 2006, **110**, 23944–23950.
- 85 I. B. Moroz, K. Larmier, W.-C. Liao and C. Coperet, *J. Phys. Chem. C*, 2018, **122**, 10871–10882.
- 86 H. Geen, J. J. Titman, J. Gottwald and H. W. Spiess, *Chem. Phys. Lett.*, 1994, **227**, 79–86.
- 87 M. B. Legrady, D. M. Dawson, P. B. Webb and S. E. Ashbrook, *Insight into the Atomic-Level Structure of  $\gamma$ -Alumina Using a Multinuclear NMR Crystallographic Approach (dataset)*, University of St Andrews Research Portal, 2025, DOI: [10.17630/5020123c-d803-4bfd-8228-3e2507f077e4](https://doi.org/10.17630/5020123c-d803-4bfd-8228-3e2507f077e4).

